Polyamines buffer labile iron to suppress ferroptosis

Pushkal Sharma[1,2], Heather R. Keys[1], Sebastian Müller[3], Ivan S. Pires[2,4], Ryan Mansell[4,5], Shinya Imada[4], Tenzin Kunchok[1], Millenia Waite[1], Christalyn Ausler[1], Bingbing Yuan[1], Amy Deik[6], Paula T. Hammond[2,4], Raphaël Rodriguez[3], Whitney Henry[4,5], Ankur Jain[1,5]

[1] Whitehead Institute for Biomedical Research, Cambridge, MA, USA

[2] Department of Chemical Engineering, Massachusetts Institute of Technology, Cambridge, MA, USA

[3] Institut Curie, CNRS, INSERM, PSL Research University, Paris, France

[4] Koch Institute for Integrative Cancer Research at MIT, Cambridge, MA, USA

[5] Department of Biology, Massachusetts Institute of Technology, Cambridge, MA, USA

[6] Broad Institute of MIT and Harvard, Cambridge, MA, USA

Lead contacts: A.J. (ajain@wi.mit.edu) or W.H. (wshenry@mit.edu)

Summary

Polyamines are essential and evolutionarily conserved metabolites present at millimolar concentrations in mammalian cells. Cells tightly regulate polyamine homeostasis through complex feedback mechanisms, yet the precise role necessitating this regulation remains unclear. Here, we show that polyamines function as endogenous buffers of redox-active iron, providing a molecular link between polyamine metabolism and ferroptosis. Using genome-wide CRISPR screens, we identified a synthetic lethal dependency between polyamine depletion and the key ferroptosis suppressor, GPX4. Mechanistically, we show that polyamine deficiency triggers a redistribution of cellular iron, increasing the labile iron pool and upregulating ferritin. To directly visualize this iron buffering in living cells, we developed a genetically encoded fluorescent reporter for redox-active iron. Live-cell analysis revealed a striking inverse correlation between intracellular polyamine levels and redox-active iron at single-cell resolution. These findings reposition polyamines as key regulators of iron homeostasis, with implications for ferroptosis-linked disease states and cellular redox balance.

Introduction

Polyamines are essential, evolutionarily conserved metabolites found in nearly all living organisms[1]. The major polyamines in mammals are putrescine, spermidine, and spermine (Figure 1A). These small molecules represent some of the most abundant metabolites in mammalian cells, reaching intracellular concentrations in the millimolar range[1]. At physiological pH, their amine groups are positively charged, enabling interactions with nucleic acids, proteins, and other negatively charged molecules, with the majority of the cellular polyamine pool associating with RNA[2].

In mammals, polyamines are derived from both de novo biosynthesis and external sources through dietary intake and cellular import[1] (Figure 1B). Cells invest heavily in regulating polyamine homeostasis, maintaining intracellular concentrations in a narrow range through an elaborate feedback network involving biosynthesis, catabolism, and transport. Ornithine decarboxylase (ODC1), the rate-limiting enzyme in polyamine biosynthesis, has one of the shortest half-lives of any mammalian protein[3]. ODC1 activity is uniquely regulated by antizyme (OAZ1), which binds ODC1 and targets it for ubiquitin-independent proteasomal degradation[4]. When polyamine levels rise, they induce a +1 ribosomal frameshift during OAZ1 translation, enabling production of functional antizyme that targets ODC1 for degradation, thereby creating a negative feedback loop. Polyamine levels are further tuned by spermidine/spermine N^1-acetyltransferase (SAT1) that acetylates polyamines for export or back-conversion[5], and polyamine oxidases that catalyze interconversion between polyamine species[6]. Polyamine import and export mechanisms are also under feedback control, though the mammalian polyamine transporters remains incompletely characterized[1]. Perturbations to cellular polyamine levels, whether genetic, pharmacologic, or environmental, trigger a rapid and coordinated response that restores intracellular polyamine homeostasis[1].

This sophisticated regulatory architecture raises a central, unresolved question: why do cells maintain polyamines at millimolar concentrations and encode such extensive regulatory pathways to monitor and control their levels? The precise molecular functions of polyamines remain poorly defined. One of the best-characterized roles is the hypusination of eIF5A, a unique, spermidine-dependent post-translational modification that is essential for translation[7]. However, hypusination occurs at sub-micromolar substrate concentrations[7] and does not explain the enormous metabolic investment in maintaining millimolar polyamine levels or justify the elaborate regulatory networks devoted to their control.

Even modest perturbations in polyamine levels can trigger cascading defects across multiple cellular pathways. Polyamine dysregulation affects chromatin compaction[8], cell differentiation[9], tissue regeneration[10], autophagy[11], and immune function[12]. These pleiotropic effects suggest that polyamines serve critical roles beyond hypusination, yet the molecular mechanisms underlying most of these functions remain undefined. Clinically, polyamine metabolism is intimately linked to human health and disease. Polyamine levels decline with age, while dietary supplementation in model organisms improves memory[13], cardiac function[14], and lifespan[15]. Conversely, polyamine pathway activation supports tumor proliferation, and elevated levels of polyamines and their biosynthetic enzymes are frequently observed across many cancers[16]. Mutations in polyamine pathway genes cause disorders such as Parkinsonian syndromes[17], Snyder-Robinson syndrome[18] and Bachmann-Bupp syndrome[19], further emphasizing their clinical importance.

Polyamine metabolism is an attractive therapeutic target, particularly in cancer where polyamine addiction drives tumor growth. However, efforts to therapeutically modulate polyamine levels have been hampered by our incomplete understanding of their function and the robust compensatory mechanisms that maintain polyamine homeostasis. For example, when polyamine biosynthesis is blocked, cells upregulate import pathways to maintain intracellular levels[20]. This metabolic plasticity has rendered single-agent polyamine depletion strategies, like DFMO (difluoromethylornithine), largely ineffective in clinical settings. To identify cellular dependencies that emerge during polyamine stress, we performed a genome-wide CRISPR-Cas9 screen[21,22] in human cells under polyamine-depleted conditions. We reasoned that this approach would reveal synthetic lethal interactions, i.e., genes and pathways that become essential only when polyamine homeostasis is disrupted, thereby uncovering both fundamental polyamine functions and potential therapeutic targets.

Our screen revealed a surprising link between polyamines and iron homeostasis. Polyamine depletion rendered cells highly dependent on GPX4 (glutathione peroxidase 4), an antioxidant enzyme that protects membranes from lethal lipid peroxidation and ferroptotic cell death[23,24]. This dependency stems from an increase in intracellular reactive iron pools upon polyamine depletion. Previous biochemical studies have shown that polyamines can coordinate metal ions such as Fe^{2+} through stable Werner-type complexes[25–32]. To test whether polyamines buffer iron in living cells, we developed a genetically

encoded sensor for labile iron. This sensor directly captured iron liberation following acute polyamine depletion, demonstrating that polyamines function as an endogenous iron buffer.

Our work adds a new dimension to our understanding of polyamine function. Beyond their roles in translation[7] and chromatin regulation[33], they also maintain redox homeostasis by buffering reactive metal ions. This metabolic dependency creates a targetable vulnerability: cells reliant on polyamine metabolism exhibit increased sensitivity to ferroptosis. By positioning polyamines at the intersection of metal homeostasis and redox biology, our findings open new therapeutic avenues for inducing synthetic lethality through combined targeting of polyamine metabolism and ferroptotic pathways.

CRISPR screen identifies genetic dependencies under polyamine depletion

The polyamine biosynthetic pathway involves two rate-limiting steps: the formation of putrescine by ODC1, and the generation of aminopropyl donors by AMD1, which are then incorporated into spermidine and spermine[1]. Polyamine depletion using the ODC1 inhibitor DFMO or the AMD1 inhibitor sardomozide, induces cytostasis without causing substantial cell death (Figure 1C). To identify genetic dependencies under varying polyamine levels, we conducted a genome-wide CRISPR-Cas9 knockout screen in K562 cells (Figure 1D). Cells transduced with a CRISPR sgRNA library[34] targeting ~20,000 protein-coding genes (5 sgRNAs per gene) were cultured with or without DFMO for 14 days. Polyamine depletion following DFMO treatment was confirmed via enzymatic assay (Figure S1A), and sgRNA abundance was compared between treated and untreated conditions using the Robust Rank Aggregation (RRA) algorithm[35] (Table S1).

Most genes scored similarly across both conditions, but several displayed selective depletion or enrichment upon polyamine depletion. Notably, loss of genes related to polyamine biosynthesis, including ODC1 and SMS (spermine synthase) sensitized cells to DFMO treatment, validating our screening approach (Figure 1E-F). This analysis identified ATP13A3, BCL2L1, and GPX4 as the top synthetic lethal hits, showing the strongest fitness defects (by p-value) upon polyamine depletion (Figure 1E-F). In contrast, knockout of the membrane proteins SLC3A2 and SLC7A6 enhanced survival under DFMO treatment (Figure 1F), likely reflecting their roles in polyamine export. SLC3A2 is an adapter protein that regulates several amino acid transporters and promotes polyamine excretion[36]. SLC7A6 forms a complex with SLC3A2[37] and likely shares this polyamine export function.

The synthetic lethality of ATP13A3, a known polyamine transporter[38], likely reflects its role in the uptake of residual polyamines from the cell culture medium. Combined inhibition of polyamine synthesis (via DFMO) and transport (via ATP13A3 knockout) could fully deplete intracellular polyamines, inducing cell death. BCL2L1 and GPX4, two additional top hits, are key survival factors in distinct cell death pathways. BCL2L1 encodes an anti-apoptotic protein that has been shown to bind and regulate voltage-dependent anion channel (VDAC) and mitochondrial membrane potential[39]. GPX4 is a lipid quality control factor that inhibits phospholipid peroxidation, and is a central regulator of ferroptosis: an iron-dependent cell death pathway characterized by lipid peroxidation[23,24].

We validated these findings using sardomozide, another polyamine biosynthesis inhibitor which targets AMD1 and blocks spermidine and spermine synthesis. Notably, this mechanism is distinct from that of DFMO, which targets ODC1 and inhibits putrescine production. Sardomozide induced substantial cytotoxicity in GPX4 knockout cells but not in control cells targeted at the AAVS1 safe-harbor locus (Figure 1G). Notably, GPX4 knockout cells proliferated slower than AAVS1 targeting cells (data not shown). Similarly, pharmacological inhibition of BCL2L1 with A-1331852 sensitized cells to polyamine depletion (Figure 1H). Notably, inhibition of GPX4 or BCL2L1 alone did not cause cell death, confirming synthetic lethality. Given the central role of GPX4 in preventing ferroptosis, we focused on understanding how polyamine depletion primes cells for this iron-dependent form of cell death.

Polyamine depletion sensitizes cells to ferroptosis

We next investigated the mechanism underlying synthetic lethality between polyamine depletion and GPX4 loss. Co-treatment with AMD1 inhibitor sardomozide and GPX4 inhibitors (ML162 or RSL3), led to substantial cell death whereas individual treatments did not (Figure 2A). Importantly, spermidine supplementation largely rescued sardomozide-induced cell death (Figure 2B), validating that the synthetic lethality results from on-target inhibition of polyamine biosynthesis. Sardomozide is a polyamine analog (Figure S1B) and competes with spermidine for uptake by the polyamine import machinery (Figure S1C, see “Polyamine import measurements” in Methods). As a result, exogenous spermidine does not fully restore intracellular polyamine levels, explaining the incomplete rescue. Interestingly, high concentrations of polyamines in the medium re-sensitized cells to ferroptosis (Figure 2B). This enhanced sensitivity to ferroptosis upon high-dose polyamine supplementation has been

reported previously[40] and likely results from the oxidation of excess polyamines by serum and cellular polyamine oxidase enzymes, that generates reactive oxygen species (ROS)[6] and potentiate ferroptotic cell death.

Building on our pharmacological data, we used genetic perturbations to dissect the contribution of individual polyamines to ferroptosis sensitivity. GPX4 inhibition induced substantial cell death in spermidine synthase (SRM) knock-out cells (Figure 2C) but not in control AAVS1-targeted cells. SRM knockout depletes both spermidine and spermine, resulting in the accumulation of the diamine putrescine. This vulnerability was rescued by spermidine supplementation, confirming the on-target activity of Cas9 (Figure 2D). In contrast, SMS (spermine synthase) knockout cells, which lack spermine but accumulate spermidine due to blocked conversion, were resistant to GPX4 inhibition (Figure 2C). SRM and SMS knockouts were confirmed by immunoblotting (Figure 2D). These results suggest that spermidine is sufficient to protect against ferroptosis, while putrescine alone cannot maintain viability under GPX4 inhibition. While spermine depletion alone does not sensitize cells to ferroptosis, its role under physiological conditions cannot be excluded.

We tested whether specific ferroptosis inhibitors could rescue cell death in polyamine-depleted cells. Treatment with known ferroptosis inhibitors, including lipophilic antioxidants[41] ferrostatin-1 and liproxstatin-1 (recently also shown to act as an iron chelator[42]), fully rescued GPX4 knockout cells from polyamine deprivation-induced death (Figure 2E). In contrast, inhibitors targeting other cell death pathways – such as apoptosis (z-VAD-FMK[43]), cuproptosis (tetrathiomolybdate[44]), and general oxidative stress (cell-permeable glutathione) – were ineffective (Figure 2E). Peroxidized lipid levels, assessed using BODIPY-C11 probe[45], were comparable across untreated controls, polyamine-deficient cells (sardomozide-treated), and GPX4 knockout cells (Figure 2F). However, brief GPX4 inhibition (~3 h, ML162) in polyamine-deficient cells markedly increased lipid peroxidation, consistent with ferroptotic lipid damage (Figure 2F). This polyamine-ferroptosis connection extended across multiple cell types: polyamine depletion enhanced ferroptosis sensitivity in NOMO (human monocytic leukemia) and HEL (human erythroleukemia) and MEL (mouse erythroleukemia) cells (Figure 2G-H, Figure S1D). Collectively, these results establish that polyamine depletion, specifically the loss of spermidine and/or spermine, creates a metabolic state selectively vulnerable to ferroptosis.

Effects of polyamines are independent of major ferroptosis regulators

Having established that polyamine depletion sensitizes cells to ferroptosis, we sought to determine the underlying mechanisms. Interestingly, while our data demonstrate that polyamine depletion sensitizes cells to ferroptosis, recent studies have shown that excess intracellular polyamines can also promote ferroptosis[40,46]. Excess spermidine and spermine are catabolized by the enzymes spermine oxidase (SMOX) and polyamine oxidase (PAOX), which convert them into lower-order polyamines such as putrescine while generating hydrogen peroxide and reactive aldehydes as byproducts[6]. These reactive intermediates can propagate lipid peroxidation, thereby sensitizing cells to ferroptotic cell death[40,46]. Consistent with this biphasic effect, we found that high-dose spermidine supplementation (100 μM) increased susceptibility of GPX4 inhibition. In sharp contrast, lower concentrations used in our rescue experiments (10 μM), which are closer to the physiological extracellular levels[47], were protective (Figure 3A). These findings suggest that both polyamine excess and deficiency can sensitize cells to ferroptosis, albeit through distinct biochemical routes, underscoring the importance of maintaining polyamine homeostasis.

Next, we tested whether polyamines function as direct antioxidants. Early studies proposed that polyamines, particularly spermidine and spermine, could act as radical scavengers and protect cells from oxidative damage[48,49]. However, their ability to scavenge lipid peroxyl radicals, the key propagating species in ferroptosis, remained untested. To address this, we evaluated whether polyamines can trap lipid peroxyl radicals using the fluorescence-enabled inhibited autoxidation (FENIX) assay[50]. This assay monitors lipid peroxidation in native liposomes by tracking the oxidation of STY-BODIPY, a lipophilic fluorophore that is quenched upon reaction with lipid peroxyl radicals. Radical-trapping antioxidants compete with STY-BODIPY, thereby preserving fluorescence. Under our experimental conditions, polyamines did not exhibit any measurable lipid radical trapping activity (Fig. 3B, Figure S1E). In contrast, PMC (2,2,5,7,8-pentamethyl-6-chromanol), a truncated vitamin E analog, robustly preserved fluorescence by intercepting lipid peroxyl radicals as expected (Figure 3B).

Since polyamines have also been proposed to broadly scavenge reactive oxygen species (ROS)[51], we tested if polyamine depletion compromises cellular antioxidant defenses, thereby increasing sensitivity to ferroptosis. To assess this, we measured total intracellular ROS levels using CM-H_2DCFDA, a broad-spectrum ROS sensor that fluoresces upon oxidation by hydrogen peroxide and related ROS[52]. Tert-

butyl hydroperoxide, a cell-permeable organic peroxide that induces peroxyl and alkoxyl radicals, served as a positive control. Interestingly, polyamine-deficient cells showed decreased ROS levels compared to controls (Figure 3C). This observation aligns with a recent study reporting that ODC1 knockout leads to lower intracellular H_2O_2 levels[40]. Additionally, polyamine depletion led to only modest changes in the mRNA abundance of downstream targets of NRF2 transcription factor, the key sensor of oxidative stress[53] (Figure S1F). Together, these results rule out a simple model where polyamine depletion promotes ferroptosis through loss of radical scavenging activity or compromised antioxidant defenses.

Having ruled out direct antioxidant mechanisms, we next tested whether polyamine depletion sensitizes cells to ferroptosis by altering known regulators of the pathway. Besides GPX4, two key regulators of the ferroptosis pathway are: ACSL4 (acyl-CoA synthetase long-chain family member 4) which enriches membranes with polyunsaturated fatty acids that serve as peroxidation substrates[54], and FSP1 (ferroptosis suppressor protein 1) which suppresses ferroptosis independently of GPX4 by regenerating ubiquinol, a lipid-soluble antioxidant that traps/scavenges lipid peroxyl radical, thereby inhibiting propagation of lipid peroxidation[55,56]. Western blot analysis revealed that the expression levels of ACSL4 and FSP1 were largely unaffected by polyamine depletion (Figure 3D-E). Interestingly, GPX4 expression increased upon polyamine depletion (Figure 3D, bottom), possibly suggesting a compensatory response to heightened ferroptosis vulnerability.

Given that polyamine depletion specifically sensitizes cells lacking GPX4, we hypothesized that polyamines might act through or converge with the FSP1 pathway. If so, FSP1 inhibition would be expected to mimic the ferroptosis-sensitizing effect of polyamine depletion. However, treating GPX4 knockout cells with the selective FSP1 inhibitor iFSP1 did not affect cell viability (Figure 3F). These findings suggest that the ferroptosis vulnerability induced by polyamine depletion is unlikely to be driven by impaired FSP1-mediated protection.

We next examined whether polyamine depletion sensitizes cells to ferroptosis through effects on polyamine-dependent cellular processes. Spermidine is required for an essential post-translational modification, hypusination, of eIF5A. Hypusinated eIF5A plays multiple roles in mRNA translation including elongation, termination, and start codon selection[57,58]. If reduced hypusination underlies

ferroptosis sensitivity, then polyamine depletion should decrease hypusinated eIF5A levels. However, immunoblot analysis revealed that acute sardomozide treatment under our assay conditions maintained normal levels of hypusinated eIF5A (Figure 3G), likely because the existing hypusinated pool is stable and cellular spermidine was incompletely depleted. Interestingly, direct hypusination blockade with GC7 did sensitize cells to ML162-induced ferroptosis, an effect rescued by liproxstatin-1 (Figure S1G). This suggests that while chronic hypusination loss can promote ferroptosis, it does not explain the acute effects of polyamine depletion in our system.

Finally, we tested whether ferroptosis sensitivity arises from polyamine depletion-induced cell cycle arrest. In certain contexts, G1/S arrest promotes ferroptosis by downregulating the phospholipid remodeling enzymes MBOAT1 and EMP2[59]. However, direct cell cycle inhibition with palbociclib, which effectively arrested cells in G1 (Figure S1H), failed to sensitize them to ML162 treatment (Figure 3H). This demonstrates that cell cycle arrest per se is not sufficient to promote ferroptosis in our system. Additionally, we did not detect ALOX15 expression by RNA-seq in our cell lines, a lipoxygenase previously implicated in polyamine catabolism-induced ferroptosis[60].

Collectively, these experiments provide strong evidence that the ferroptosis-sensitizing effects of polyamine depletion are not mediated by these known regulatory pathways such as FSP1, hypusination-dependent translation, or cell cycle arrest. The protective effects of polyamines also cannot be attributed to direct radical scavenging or general antioxidant activity. While we cannot fully exclude contributions from these pathways, our findings strongly suggest that polyamine deficiency enhances ferroptosis susceptibility through a mechanism distinct from these established routes.

Polyamines can chelate metal ions

Having established that polyamines protect against ferroptosis through a mechanism independent of known regulatory pathways, we next examined upstream processes that might explain this vulnerability. Given that ferroptosis is fundamentally driven by iron-catalyzed lipid peroxidation, we examined potential connections between polyamine metabolism and cellular iron homeostasis. Polyamines can directly chelate metal ions: the nitrogen atoms on the amine groups bear lone pairs of electrons that can coordinate vacant orbitals in metal ions, forming stable Werner-type coordination complexes. Studies dating back to the 1950s demonstrated that neutralized polyamines can form stable complexes with

various transition metals, including copper, nickel, cobalt, lead, and zinc[25–32]. Structural analysis using X-ray crystallography shows that spermine coordinates copper with its nitrogen donors arranged in a square-planar geometry around the central metal ion[61]. This structure strongly resembles the metal-binding architecture observed in other nitrogen-containing biological macrocycles such as chlorophyll and porphyrins[62].

Despite these in vitro observations, the biological relevance of polyamine metal-binding has remained unclear. At physiological pH, polyamines are expected to be protonated and lack available lone electron pairs for metal coordination. However, in cells, polyamines are extensively complexed with negatively charged biomolecules, including nucleic acids, ATP, and acidic phospholipids[2]. These electrostatic interactions may shift the local protonation equilibria of polyamines, partially unmasking nitrogen lone pairs and enabling metal ion coordination[63,64]. Indeed, polyamines have been shown to form ternary complexes with metals and phosphate-containing compounds (ATP, RNA, phospholipids[31,65]) *in vitro*. These complexes stabilize iron in a less redox-active state that inhibits Fe^{2+} autoxidation[66,67] and prevents lipid peroxidation *in vitro*[68,69].

The therapeutic use of trientine[70], a linear tetraamine structurally similar to spermine (Figure S2F), further supports the potential for polyamine-based metal chelation. Trientine is the first-line treatment for copper toxicity and Wilson's disease. It effectively chelates copper, forming stable coordination complexes that are excreted in the urine, thereby lowering systemic copper levels. Notably, patients treated with trientine often exhibit side effects associated with iron deficiency, suggesting that it has broader metal-chelating properties beyond copper[71,72].

Multiple lines of evidences also indicate extensive metabolic cross-talk between polyamine and iron homeostasis. Analysis of the Cancer Dependency Map showed a striking correlation between cellular dependencies on AMD1, a rate-limiting enzyme in polyamine biosynthesis, and TFRC (transferrin receptor), the major mediator of cellular iron import (Pearson's correlation coefficient, $r = 0.422$, across $n = 1149$ cell lines) (Figure 4A). This co-dependency was particularly pronounced in iron-sensitive lineages including prostate ($r=0.906$, $n=10$), bladder/urinary tract ($r= 0.711$, $n=34$), eye ($r=0.746$, $n=15$), head and neck ($r=0.617$, $n=74$) and skin ($r=0.605$, $n=74$) cancer lineages (Figure S2A-E), indicating that

cells with high iron demand (reflected by TFRC dependence) exhibit an increased reliance on robust polyamine synthesis.

Notably, iron depletion lowers intracellular spermidine and spermine levels[73], while iron overload activates polyamine biosynthesis through upregulation of ODC1[40]. Clinically, polyamine depletion using drugs such as DFMO, frequently causes side effects tied to iron dysregulation, including anemia and thrombocytopenia[74]. Loss of function mutations in ATP13A2, a polyamine transporter linked to early-onset Parkinson's disease, lead to iron accumulation in basal ganglia and cultured dopaminergic neurons[75–78]. Notably, before ATP13A2 was recognized as a polyamine transporter, it was shown to protect cells against metal-induced toxicity, including from Fe^{3+}, Mn^{2+}, and Zn^{2+}[79–83]. Similarly, loss-of-function mutations in ATP13A3, the primary polyamine transporter in non-neuronal cells[84], are associated with pulmonary arterial hypertension (PAH)[85], a disease frequently characterized by disruption of iron metabolism[86]. Together, these observations indicate extensive metabolic cross-talk between polyamine and iron homeostasis, leading us to hypothesize that polyamines may function as endogenous iron buffers in cells, and that polyamine depletion enhances ferroptosis by increasing labile iron pools.

Polyamine deficiency increases redox-active iron in cells

If polyamines directly chelate iron in cells, their depletion should destabilize iron homeostasis. Consistent with this notion, we observed that polyamine depletion using sardomozide resulted in a dramatic increase in levels of ferritin (FTH1), the principal iron storage protein[87,88] (Figure 4B). This induction mirrored the response to exogenous iron supplementation, such as with ferric ammonium citrate (FAC) or ferrous ammonium sulfate (FAS) (Figure S2G). Similar ferritin upregulation was observed upon SRM knock out and was reversed by exogenous spermidine supplementation (Figure 4C).

Ferritin sequesters iron in an insoluble, non-reactive form, mitigating the risk of excessive redox-active iron accumulation[87]. We hypothesized that ferritin upregulation in polyamine-deficient cells represents an adaptive response to increased redox-active iron. Supporting this hypothesis, treatment with deferoxamine (DFO), an iron chelator, blunted the increase in ferritin levels from polyamine depletion (Figure 4D). Direct measurement using lysosomal ferrous-specific fluorescent probe RhoNox-M[125]

confirmed elevated intracellular ferrous iron levels upon polyamine depletion (Figure 4E), similar to those observed upon treatment with ferric ammonium sulfate (Figure 4E).

To investigate the functional consequences of elevated redox-active iron upon polyamine depletion, we tested whether its modulation could rescue cell viability. Indeed, DFO treatment restored viability in polyamine-deficient cells, either treated with sardomozide or lacking SRM, challenged with the GPX4 inhibitor ML162 (Figure 4F-G). Although precise normalization of intracellular iron concentrations to baseline is experimentally challenging, the rescue by iron chelation strongly supports iron accumulation as a key driver of ferroptosis susceptibility. To further validate the link between increased redox-active iron and ferroptosis, we directly increased the redox-active iron pool using ferric ammonium citrate (FAC). FAC supplementation induced cell death specifically in GPX4 knockout cells, and this effect was fully rescued by the ferroptosis inhibitor liproxstatin-1 (Figure 4H). Importantly, FAC had no impact on the viability of cells with functional GPX4 (Figure 4H), indicating that excess iron is not inherently toxic but becomes lethal when lipid peroxide repair is compromised. Collectively, these findings strongly implicate increased redox-active iron accumulation as a critical mediator of ferroptosis under polyamine-deficient conditions.

We next investigated the source of increased intracellular redox-active iron. We first examined if polyamine depletion results in increased iron uptake from the culture medium. Interestingly, total intracellular iron levels, as measured by inductively coupled plasma mass spectrometry (ICP-MS), decreased rather than increased upon polyamine depletion (Figure 4I). This observation indicates that the increase in the redox-active iron does not result from increased total iron but rather reflects a shift in the redox state or subcellular distribution of existing iron pools. Supporting this conclusion, ferritin levels were elevated even when polyamine-deficient cells were cultured in iron-free medium (IMDM) following extensive washing to remove extracellular iron (Figure 4J). Polyamine depletion also did not reduce intracellular levels of known intracellular iron ligands[89], including GSH, ATP, and citrate, as determined by metabolite analysis (Figure 4K).

The disruption of iron homeostasis upon polyamine depletion was conserved across diverse cell types. Sardomozide treatment increased ferritin levels in U-2OS (osteosarcoma), RPE-1 (retinal pigment epithelial) and MRC-5 (fetal lung fibroblast) cells (Figure 4L). Similarly, DFMO treatment elevated

ferritin levels in mouse colon cancer organoids with *Apc* mutations (APC) alone or in combination with *Kras*^{G12D}, and *Trp53* mutations (AKP, a genotype observed in 40–45% of patients with colorectal cancers[90,91]) (Figure 4M). These results underscore that the disruption of iron metabolism due to polyamine deficiency is a conserved phenomenon across different cellular contexts. Taken together, these findings establish that polyamine depletion disrupts cellular iron homeostasis, creating a metabolic vulnerability that renders cells dependent on GPX4 for survival.

Genetically encoded iron sensor reveals polyamine-iron buffering in living cells

Our findings point to a model where polyamines function as an endogenous iron buffer system: at millimolar concentrations, they sequester redox-active iron in stable coordination complexes, preventing its participation in harmful Fenton chemistry. This model predicts that polyamine depletion liberates sequestered iron, explaining the increased ferritin expression and ferroptosis sensitivity. However, direct visualization of this iron liberation in living cells is technically challenging. Existing methods using fluorescent dyes lack quantitative reliability as the signal is affected by local pH, ionic environment, and interference from other metals including zinc and copper. Furthermore, their limited cell permeability, poor photostability, and rapid clearance make them unsuitable for long-term imaging or analysis in complex tissues and organoids.

To overcome these limitations and directly test our iron-buffering hypothesis, we developed a genetically encoded reporter that quantifies redox-active iron in living cells with single-cell resolution. We harnessed the endogenous iron-responsive element (IRE)/iron regulatory protein (IRP) system: an evolutionarily conserved mechanism that exquisitely monitors and regulates the labile iron pool[92]. IRPs bind to IRE hairpins in mRNAs encoding key iron regulatory proteins. When iron is low, IRP binding to 5′ UTR IREs (such as in ferritin and ferroportin mRNAs) blocks their translation, thus inhibiting iron sequestration and export. Conversely, IRP binding to IREs in 3'UTRs (such as in transferrin receptor mRNA) enhance transcript stability and translation, thereby promoting iron uptake. When labile iron concentrations rise, iron-sulfur clusters assemble on IRP1 while IRP2 undergoes degradation, releasing both proteins from their RNA targets and reversing this regulatory program.

We exploited this nature's own iron-sensing switch to engineer a genetically encoded fluorescent reporter (Figure 5A). We incorporated an optimized IRE configuration (Supplementary Note 1, Figure

S3A–C) upstream of EBFP2 coding sequence. Translation initiation of EBFP2 depends directly on IRP release, providing a sensitive indicator of cellular redox-active iron. Additionally, we included an internal ribosome entry site (IRES)-mediated expression of EGFP downstream of EBFP2 as an internal normalization control, effectively accounting for cell-to-cell variability in mRNA abundance, transduction efficiency, and general translational status (Figure 5B). The fluorescence ratio of EBFP2 to EGFP provided a sensitive and quantitative measure of intracellular redox-active iron levels. Sensor expression was further refined by placement under a doxycycline-inducible promoter, enabling tight temporal control and preventing saturation of the sensor's dynamic range with prolonged expression. Importantly, reporter expression did not perturb endogenous iron metabolism, as evidenced by unchanged protein levels of iron metabolism enzymes, including FTH1, TFR1 and SLC40A1 (Figure S3D).

To validate the reporter, we measured changes in the fluorescence ratio (F = EBFP2/EGFP), normalized to untreated cells (F_0), to correct for imaging variations, as a function of redox-active iron. Treatment with the iron chelator DFO (100 μM, 48 h) markedly reduced this normalized fluorescence ratio by ~2.8 fold ($F/F_0 = 0.36 \pm 0.10$ compared to the baseline levels of 1.00 ± 0.23), consistent with reduced intracellular redox-active iron. Supplementation with ferric ammonium citrate (FAC, 10 mM, 18 h) partially restored the signal ($F/F_0 = 0.70 \pm 0.16$) (Figure 5C-D), confirming the sensor's responsiveness to iron availability. Similar trends were observed in K562 cells (Figure 5E).

We next leveraged our reporter to investigate the relationship between polyamine levels and redox-active iron. Treatment with sardomozide (5 μM for 48 h) or DFMO (0.5 mM for 48 h) led to a significant increase in F/F_0 (from 1.00 ± 0.23 to 2.22 ± 0.81 for sardomozide and 1.74 ± 0.45 for DFMO treatments respectively) (Figure 5F), indicating an increase in redox-active iron levels. Co-treatment with the iron chelator DFO (100 μM for 48h) reversed this elevation, confirming that the signal reflected iron-dependent changes (Figure 5E). Similar iron accumulation upon polyamine depletion was observed in K562 cells (Figure 5G), reinforcing the link between polyamine availability and the labile iron pools.

To definitively link these two metabolic pools at a single-cell level, we implemented a dual-reporter strategy. We co-expressed our iron sensor alongside a genetically encoded polyamine reporter we recently developed[84]. This sensor employs a polyamine-responsive ribosomal frameshifting region

derived from OAZ1 gene cloned between two fluorescent proteins, mCherry and miRFP670-2 (Figure 5H). In this design, miRFP670-2 is produced only upon polyamine-stimulated frameshifting, providing a direct readout of intracellular polyamine concentrations, while mCherry serves as an internal normalization control.

This dual-reporter approach enabled the simultaneous and quantitative measurement of both pathways within individual cells. We treated cells with a titration of sardomozide to induce a range of intracellular polyamine concentrations, and then captured both the polyamine and iron sensor signals on a single-cell basis (Figure 5I-J). Strikingly, we observed a robust inverse relationship between the two reporter readouts (Pearson's correlation coefficient, r, between $(F/F_0)_{iron}$ and $(F/F_0)_{polyamine}$ = -0.91), confirming that polyamine depletion is proportionally coupled to an increase in redox-active iron (Figure 5K).

Collectively, these findings demonstrate a direct and reciprocal relationship between cellular polyamine abundance and redox-active iron. Our data support a model where polyamines act as a physiological buffer for labile iron, stabilizing it in non-reactive complexes and thereby preventing oxidative damage. Disruption of this buffering system through polyamine depletion liberates iron from these complexes, elevating the bioavailable iron pool and sensitizing cells to ferroptotic death. By enabling dynamic, single-cell resolution tracking of iron metabolism, our genetically encoded reporter provides a powerful new tool for dissecting iron biology in diverse physiological and disease contexts. More broadly, these findings uncover an unexpected layer of iron regulation by polyamines, linking two fundamental metabolic networks with relevance to redox stress, cell death, and metabolic disease.

Discussion

Our discovery that polyamines regulate iron homeostasis and ferroptosis sensitivity is timely and holds significant implications for numerous ongoing trials investigating polyamine depletion in cancer therapy and other diseases (e.g., NCT06892678 for Ewing sarcoma, NCT05594563 for type 1 diabetes, NCT04301843 for neuroblastoma, NCT04696029 for medulloblastoma, NCT06976424 for hirsutism). An elevated rate of polyamine biosynthesis is a metabolic hallmark of rapid cellular proliferation and growth. This metabolic phenomenon has long been observed in cancer cells and tumors. For example, comparative RNA-seq analyses[93] highlight a striking upregulation of polyamine biosynthesis enzymes (e.g., ODC1, SRM) in tumors compared to paired normal tissues (Figure S4A-B, Table S3). This

reprogramming is driven by oncogenic signaling pathways, such as MYC[94], RAS-RAF-MEK[95,96], AKT[97], and mTORC1[98], which converge to sustain polyamine production. Importantly, this metabolic shift is not merely a byproduct of these pathways but is essential for the tumorigenic activity of many of these oncogenes[99,100]. Beyond primary tumor growth, polyamines are also critical for metastatic dissemination[101–105] and immune evasion[106]. While FDA-approved drugs like DFMO, which deplete polyamines, have shown promise in neuroblastoma maintenance therapy[107] and chemoprevention[108], their standalone efficacy against cancer has been limited[109]. Our results identify several novel actionable targets (GPX4, BCL2L1 and ATP13A3), providing a foundation for combination therapies to enhance the efficacy of polyamine depletion in cancer treatment. While this manuscript was under preparation, another study reported that DFMO prevents metastasis in Ewing sarcoma by inducing ferroptosis signatures[110], reinforcing the therapeutic relevance of our findings.

Additionally, we developed a novel genetically encoded fluorescent reporter that enables quantitative measurement of redox-active iron levels in living cells at single-cell resolution. This reporter leverages the endogenous iron-responsive RNA elements in the iron metabolism enzymes to provide a highly sensitive and dynamic readout of intracellular iron concentrations. By eliminating the need for chemical synthesis and variability associated with the traditional iron probes, this system significantly simplifies and accelerates redox-active iron measurements. Its single-cell resolution supports high-throughput screening applications and facilitates the discovery of novel regulators of iron homeostasis. Furthermore, its ability to track iron dynamics within the same sample opens the door to pharmacokinetic studies of iron-targeting therapies, potentially even in live animal models. We anticipate that this reporter will provide a powerful platform to facilitate future discoveries into iron biology and ferroptosis, advancing our understanding of disease mechanisms and potentially providing novel strategies for therapy development.

Our discovery that polyamines buffer cellular iron likely reveals an ancient metabolic partnership between two of life's most fundamental molecules. Polyamines and iron emerged early in evolution: polyamines as primordial polycations essential for RNA stability and protein synthesis, iron as the versatile redox cofactor driving cellular chemistry. As early life forms evolved to exploit iron’s catalytic power, polyamines were likely co-opted to stabilize redox-active iron and suppress its toxic potential. This dual role of polyamines in supporting macromolecular synthesis while buffering metal-induced

damage explains the extraordinary cellular investment in maintaining polyamines at millimolar levels, safeguarded by tightly regulated biosynthetic, catabolism, and transport pathways. By revealing polyamines as redox buffers, our work recasts these elaborate regulatory mechanisms as rapid-response systems for managing cellular iron. This fundamental crosstalk positions polyamine metabolism as a master regulator of ferroptosis sensitivity, with implications spanning bacterial pathogenesis, cold tolerance[111] to cancer therapy.

This polyamine-iron axis also reshapes our understanding of metabolic dysfunction in disease. Polyamine levels decline with age and this change is traditionally viewed as a passive consequence of reduced biosynthetic activity. Our findings suggest that reduced polyamine levels may result in a progressive failure in iron buffering, contributing to increased oxidative stress and vulnerability to ferroptosis[112]. Notably, recent reports indicate that aged alveolar type 2 (AT2) cells in vivo exhibit elevated labile iron levels compared to young cells, impacting stemness and tumorigenesis[113]. This may be potentially driven, at least in part, by age-related polyamine loss, although requires further investigation.

Conversely, elevated polyamine synthesis in cancer cells might serve a dual purpose: supporting rapid proliferation while simultaneously protecting against oxidative stress arising from dysregulated metabolism. For example, both polyamine[114] and iron metabolism[115–117] are upregulated in cancer stem cells. This metabolic interplay may extend beyond cancer and aging, influencing fundamental processes such as differentiation, immune responses, inflammation, and tissue regeneration, which critically depend on redox control and iron homeostasis. By establishing polyamines as intrinsic iron buffers, we illuminate a previously unrecognized layer of metabolic regulation. Understanding this partnership will be crucial for therapeutic precision, whether exploiting cancer cell dependence on polyamine-mediated iron buffering or protecting healthy tissues from ferroptotic death.

Limitations

The exact ligand composition of the redox-active iron pool in mammalian cells remains incompletely characterized. Advanced techniques such as size exclusion chromatography coupled with inductively coupled plasma mass spectrometry (SEC-ICP-MS) and Mössbauer spectroscopy, as successfully applied in bacterial systems[89], could provide deeper insights into the molecular interactions between complexed polyamines and labile iron pools in mammalian cells.

Additionally, while our study focused on the role of polyamines in iron homeostasis, other pathways may also contribute to polyamine depletion's sensitization effects on ferroptosis. Polyamine depletion also leads to cysteine depletion without impacting key reducing factors like GSH and NADPH (Figure S4C, thiols quantified by Ellman's reagent labeling followed by mass spectrometry). This was accompanied by strong transcriptional downregulation of SLC7A11 - the primary cysteine source in dividing cells - and multiple other downstream targets of ATF4 (Figure S4D), the major transcription factor regulating SLC7A11 expression. Cysteine depletion may also promote ferroptosis through its role in synthesizing GSH, coenzyme A[118] and metabolism to sulfane sulfur species[119], warranting further investigation.

Notably, polyamine depletion, achieved through either genetic or pharmacological interventions, globally increased levels of polyunsaturated phosphatidylcholines (PCs) and phosphatidylethanolamines (PEs) which could be rescued by spermidine supplementation (Figure S4E–J). These effects were independent of changes in overall abundance of lipid subtypes (Figure S4K-L) or lipid droplet accumulation[120] (Figure S4M), as assessed using BODIPY 493/503 staining, with oleic acid serving as a positive control. These lipid species are well-established substrates involved in ferroptosis[121,122] and could independently or synergistically exacerbate vulnerability to ferroptotic cell death. These effects may also in-part be related to the ability of polyamines to post-translationally modify phospholipases[123]. Further studies are needed to delineate the relative contributions of lipid processing, cysteine metabolism and iron homeostasis to ferroptosis under polyamine-deficient conditions.

Acknowledgments

We thank Matthew Vander Heiden, Lindsey Backman, Naama Kanarek, and Daniel Suess for insightful discussions. We are grateful to Punam Bisht for providing MRC-5 fibroblasts, George Bell and Xinlei Gao for assistance with data analysis, and Alex Joseph for support with plasmid preparation. We appreciate valuable feedback from Brighton A. Skeel, Ky Lowenhaupt, Mohamed El-Brolosy, Peter Tsevetkov, Reuben Saunders, Eric Smith, Sarah Willis, Walt Massefski, Mackenzie Field, and members of the Jain lab. We also thank the Flow Cytometry Core at the Whitehead Institute for assistance with flow cytometry. S.S. and R.R. acknowledge support from Ligue Contre le Cancer (Equipe Labellisée) and Fondation Charles Defforey–Institut de France. This work is supported by grants from the NIH R35GM151111 (A.J.), Bumpus Foundation (A.J.), Pew Charitable Trusts (A.J.)

Author contributions

P.S. and A.J. conceived the project. P.S. designed, performed, analyzed, and interpreted most experiments. H.R.K. helped with the CRISPR-Cas9 screen and analyzing related data. S.M., I.S.P., R.M., S.I., T.K., M.W., C.A., B.Y., A.D., P.T.H., and R.R. assisted with data acquisition and analysis. A.J. and W.S.H. supervised the project. P.S. and A.J. wrote the manuscript with inputs from all other authors.

Competing interests

A.J. and P.S. are inventors on a pending patent application based on this work. The remaining authors declare no competing financial interests.

Figure legends

Figure 1: CRISPR screen identifies modulators of polyamine sensitivity

(A) Chemical structures of mammalian polyamines.

(B) Schematic of the polyamine metabolic pathway in mammalian cells. DFMO: difluoromethylornithine, Sard: sardomozide.

(C) Cumulative population doublings of K562 cells treated with DFMO (0.5 mM), sardomozide (1 μM), and RO-3306 (5 μM, CDK1 inhibitor) over 12 days. Cells were passaged every 3 days.

(D) Schematic of the CRISPR knockout screen workflow in K562 cells.

(E) Volcano plot showing -log10 (P value) versus median log2 (fold depletion) for all genes identified in the CRISPR drop-out screen. Horizontal line: $p < 0.05$; vertical line: fold change < -1.5. Top hits are highlighted in blue.

(F) Fold change of sgRNAs targeting indicated genes. Each point represents a distinct sgRNA sequence. Error bars indicate mean ± SD (n = 5 sgRNAs).

(G) Viability of AAVS1 and GPX4 knockout (KO) K562 cells treated with sardomozide (5 μM, 96 h).

(H) Viability of K562 cells treated with A-1331852 (0.1 μM, 48 h) following pre-treatment with sardomozide (5 μM, 72 h). DMSO served as the vehicle control.

Figure 2: Polyamine depletion promotes ferroptosis

(A) Viability of K562 cells treated with ML162 (1 μM, 24 h) or RSL3 (2 μM, 24 h) following pre-treatment with sardomozide (5 μM, 96 h). DMSO served as the vehicle control.

(B) Viability of K562 cells treated with ML162 (1 μM, 24 h) following pre-treatment with sardomozide (5 μM, 72 h) and spermidine (72 h).
(C) Viability of AAVS1, SRM, and SMS knockout (KO) K562 cells treated with ML162 (1 μM, 24 h). SRM KO cells were cultured with spermidine (10 μM) that was removed 6 days before ML162 treatment.
(D) Immunoblot confirming SRM and SMS knockout in K562 cells.
(E) Viability of GPX4 KO K562 cells treated with sardomozide (5 μM, 96 h) plus ferrostatin (2.5 μM), liproxstatin (1 μM) , z-VAD-FMK (15 μM), TTM (10 μM), or GEE (100 μM) for 48 h.
(F) Lipid peroxidation measured using C11-BODIPY (581/591) in K562 cells treated with sardomozide (5 μM, 96 h) and/or ML162 (1 μM, 2.5 h). Data are presented as relative mean fluorescence intensity ± SD (n = 3 biological replicates).
(G-H) Viability of NOMO (G) and HEL (H) cells treated with ML162 (24 h) following pre-treatment with sardomozide (5 μM, 72 h). DMSO served as vehicle control.

Figure 3: Polyamines act independently of canonical ferroptosis regulators
(A) Viability of K562 cells treated with ML162 (2 μM, 24 h) following pre-treatment with spermidine (72 h).
(B) Representative fluorescence of STY-BODIPY oxidation in co-autoxidation assays (2 μM STY-BODIPY, 0.1 mM liposomal soy PC, 200 μM DTUN) with spermidine or PMC (positive control). PMC: 2,2,5,7,8-pentamethyl-6-chromanol.
(C) Relative reactive oxygen species (ROS) levels in K562 cells treated with sardomozide (5 μM, 72 h) or tert-Butyl hydroperoxide (100 μM, 3 h) via CM-H2DCFDA probe.
(D) Immunoblot of ACSL4 and GPX4 levels in K562 cells upon sardomozide treatment (5 μM, 96 h).
(E) Immunoblot of FSP1 in K562 cells treated with sardomozide (5 μM, 96 h). OVCAR8 lysate used as a positive control.
(F) Viability of GPX4 KO K562 cells treated with iFSP1 (FSP1 inhibitor) or sardomozide (5 μM, 96 h).
(G) Immunoblot showing hypusinated eIF5A levels in K562 cells treated with sardomozide (5 μM, 72 h).
(H) Viability of AAVS1 or GPX4 KO K562 cells treated with palbociclib (Pal) (10 μM, 6 days).

Figure 4: Polyamine deficiency increases redox-active iron

(A) Gene essentiality scores from Cancer Cell Line Encyclopedia for TFRC and AMD1.
(B) Immunoblot of FTH protein in K562 cells treated with sardomozide (5 μM).
(C) Immunoblot of FTH and SRM in SRM KO K562 cells; spermidine (10 μM) was removed 6 days prior to lysate collection.
(D) Immunoblot of FTH in K562 cells treated with sardomozide (5 μM, 48 h) and DFO (50 μM, 48 h).
(E) Redox-active Fe^{2+} content measured with RhoNox-M and LysoTracker in cells treated with sardomozide (5 μM, 72 h). FAS (50 μM, 5 h) as positive control.
(F) Viability of K562 cells treated with ML162 (2 μM, 24 h) and DFO (100 μM, 24 h) after pre-treatment with sardomozide (5 μM, 72 h).
(G) Viability of AAVS1 and SRM KO K562 cells treated with ML162 (2 μM, 24 h). SRM KO cells were cultured with spermidine (10 μM) that was removed 8 days before ML162 treatment. DFO (50 μM) was added 24 h prior to ML162.
(H) Viability of AAVS1 and GPX4 KO K562 cells under indicated treatment. FAC (10 mM, 96 h) and liproxstatin (2 μM, 96 h).
(I) Inductively coupled plasma-mass spectrometry (ICP-MS) quantification of cellular iron in K562 cells treated with sardomozide (5 μM, 72 h). FAC (2 mg/mL, 12 h) as positive control.
(J) Immunoblot of FTH in K562 cells in iron-free IMDM treated with sardomozide (5 μM, 48 h). Cells were washed with warm HBSS twice prior to culturing in IMDM.
(K) Relative abundance of indicated metabolites in K562 cells treated with sardomozide (5 μM, 72 h).
(L) Immunoblot of FTH in U-2OS, RPE-1 and MRC-5 cells treated with sardomozide (5 μM, 72 h). DMSO as vehicle control.
(M) Immunoblot of FTH in APC and AKP intestinal organoids treated with sardomozide (5 μM, 48 h). DMSO as vehicle control.

Figure 5: Genetically encoded sensor for redox-active iron

(A) Schematic of iron-responsive translation initiation of FTH mRNA.
(B) Design of redox-active iron sensor.
(C-D) Representative fluorescence micrographs (C) and flow cytometry quantification (D) of translation initiation efficiency (F = BFP/GFP, F_0 = F of control cells) in U-2OS cells expressing iron sensor under indicated treatments. DFO, 100 μM (48 h) and FAC, 10 mM (24 h). Median ± interquartile range from ≥

100 cells. 50 data points shown. Data: ≥2 independent experiments. Significance via paired two-tailed Student's t-test. Scale bars, 10 μm.

(E) Flow cytometry quantification of translation initiation efficiency (F = BFP/GFP) in K562 cells expressing iron sensor under indicated treatments. DFO, 50 μM (48 h) and FAC, 10 mM (24 h). Median ± interquartile range from ≥ 100 cells. 50 data points shown. Data: ≥2 independent experiments. Significance via Student's t-test.

(F-G) Flow cytometry quantification of translation initiation efficiency (F = BFP/GFP) in (F) U-2OS and (G) K562 cells expressing iron sensor under indicated treatments. Sard, 5 μM (48 h), DFMO 0.5 mM (48 h) and DFO, 100 μM (48 h). Median ± interquartile range from ≥ 100 cells. 50 data points shown. Data: ≥2 independent experiments. Significance via Student's t-test.

(H) Design for the polyamine sensor.

(I) Representative fluorescence micrographs of cells expressing polyamine sensor and iron sensor under indicated treatments. Sard, 5 μM (48 h).

(J) Change in redox-active iron (yellow) and polyamines (purple) measured using respective sensors under sardomozide treatment. Median ± interquartile range from ≥ 100 cells. 50 data points shown.

(K) Linear regression of redox-active iron and polyamine concentration (from Figure 5K).

*** means $p<0.0001$

Figure 6: Proposed model for how polyamine depletion increases ferroptotic susceptibility. Polyamine depletion frees intracellular Fe^{2+} from polyamine-iron complexes, enhancing redox-active iron pools that drive Fenton chemistry and lipid peroxidation, ultimately causing membrane rupture and ferroptotic cell death.

Methods

RESOURCE AVAILABILITY

Lead contact

Further information and requests for resources and reagents should be directed to the lead contact, Ankur Jain (ajain@wi.mit.edu) or Whitney Henry (wshenry@mit.edu).

Materials availability

All unique and stable reagents generated in this study are available from the lead contact upon completion of a Materials Transfer Agreement.

Data and code availability

CRISPR screen datasets have been deposited in the GEO database under accession number GSE300179. The mapping code for aligning sequence reads to the sgRNA library is accessible via the GitHub repository (https://github.com/whitehead/barc/tree/main/Perl). Additional information required for data reanalysis is available from the lead contact upon request.

Cell lines and organoids

U-2OS, K562, and RPE1 (immortalized) cell lines were obtained from ATCC. NOMO, HEL, and MEL cells were generously provided by Naama Kanarek (Boston Children's Hospital), and MRC-5 fibroblasts by Punam Bisht (Whitehead Institute). U-2OS, HEK293T, RPE1, and MRC-5 cells were cultured in DMEM (Gibco, Cat# 11965126), while K562, NOMO, HEL, and MEL suspension cells were maintained in RPMI-1640 (Gibco, Cat# 11875093). All media were supplemented with 10% (v/v) fetal bovine serum (FBS; Gibco, Cat# A56707-01, Lot# U2933097RP) and penicillin-streptomycin-glutamine (Gibco, Cat# 10378016). FBS was thawed at 4°C and used without further processing. For iron reporter assays, all cell types were cultured in RPMI supplemented with tetracycline-free cosmic calf serum (CCS) in place of FBS. All cell lines were maintained at 37°C in a humidified atmosphere containing 5% CO_2 and were tested monthly for mycoplasma contamination.

Lentivirus production for CRISPR-Cas9 screen

15×10^6 HEK-293T cells were seeded in T175 cm^2 flasks in DMEM (Thermo Fisher Scientific #12430054) supplemented with 10% fetal bovine serum (GeminiBio #100-106). After 24 hours, the media was changed to 20 mL viral production medium: IMDM (Thermo Fisher Scientific #1244053) supplemented with 20% inactivated fetal serum (GeminiBio #100-106). At 32 hours post-seeding, cells were transfected with a mix containing 76.8 µL Xtremegene-9 transfection reagent (Sigma Aldrich #06365779001), 3.62 µg pCMV-VSV-G (Addgene plasmid # 8454)[124], 8.28 µg psPAX2 (a gift from Didier Trono; Addgene plasmid # 12260), and 20 µg sgRNA/Cas9 plasmid and Opti-MEM (Thermo Fisher Scientific #11058021) to a final volume of 1 mL. Media was changed 16 hours later to 55 mL

fresh viral production medium. The virus was collected at 48 hours post-transfection and filtered through a 0.45 µm filter, aliquoted, and stored at -80 °C until use.

CRISPR-Cas9 screen

A genome-wide lentiviral sgRNA library[34] in a Cas9-containing vector comprising 97,888 unique sgRNA sequences with ~5 sgRNAs per target was used to transduce 390 × 10^6 K562 cells to achieve an MOI < 1 (10-20% transduction efficiency) and ~500-1000-fold library coverage. Briefly, polybrene (10 µg/mL final concentration) and virus were mixed with cells (2.5 × 10^6 cells/mL final density) and distributed into individual wells in 6-well plates. Plates were centrifuged at 1126 *g* for 45 minutes at 37 °C and transferred to an incubator. After 8 hours, cells were pelleted, the virus was removed, cells were resuspended in the fresh growth medium, and transferred to T225 cm^2 flasks (250,000 cells/mL final density). After 36 hours, cells were collected and reseeded in fresh growth medium (200,000 cells/mL final density) and puromycin was added (3 µg/mL final concentration). After 3 days, cells were collected and transduction efficiency was determined by comparison of cell survival of transduced cells relative to control cells (untransduced and unselected). Cells were passaged every 2 days (0.2 × 10^6 cells/mL) before DFMO treatment (0.5 mM) starting 9-days post-transduction. At the screen endpoint (14 days DFMO treatment), cell pellets were collected from flasks and frozen at –80 °C.

Sequencing library preparation

Genomic DNA (gDNA) was extracted from cell pellets of 20 x 10^6 cells using the Blood genomicPrep Mini Spin Kit (Cytiva # 28904264) or 60 × 10^6 cells using the QIAamp DNA Blood Maxiprep Kit (Qiagen # 51192) according to manufacturer's instructions with minor modifications: Cytiva and QIAGEN Protease were replaced with a 10 mg/mL solution of ProteinaseK (MilliporeSigma # 3115879001) in water; cells were lysed overnight; centrifugation steps after Qiagen Buffer AW1 and AW2 were performed for 2 minutes and 5 minutes, respectively; 2 x 30 µL (Cytiva) or 1 mL (Qiagen) of water preheated to 70 °C was used to elute gDNA (1- or 5-minute incubation), followed by centrifugation for 1 or 5 minutes (Cytiva or Qiagen extractions, respectively). gDNA was quantified using the Qubit dsDNA HS Assay kit (Thermo Fisher Scientific #Q32851).

All PCR reactions were performed in 50 µL reactions using ExTaq Polymerase (Takara Bio #RR001B) using the following primers:

Forward: 5'- AATGATACGGCGACCACCGAGATCTACACCCCACTGACGGGCACCGGA - 3'

Reverse: 5'- CAAGCAGAAGACGGCATACGAGATCnnnnnnTTTCTTGGGTAGTTTGCAGTTTT - 3'

Where "nnnnnn" denotes the barcode used for multiplexing.

For all samples, 1, 3, or 6 µg of gDNA was initially amplified for 28 cycles in 50 µL test PCR reactions. Subsequently, an additional 50 µL reactions were performed using 6 µg per reaction (140 µg gDNA). Reactions were pooled and 100 µL of each sample was purified using HighPrep PCR beads (MagBio Genomics #AC-60005), eluted with 20 µL water, and quantified using the Qubit dsDNA HS Assay kit before sequencing for 26 cycles on an Illumina NovaSeq using the following primers:

Read 1 sequencing primer: 5'- GTTGATAACGGACTAGCCTTATTTAAACTTGCTATGCTGTTTCCAGCATAGCTCTTAAAC - 3'

Index sequencing primer: 5'- TTTCAAGTTACGGTAAGCATATGATAGTCCATTTTAAAACATAATTTTAAAACTGCAAACTACCCAAGAAA - 3'

CRISPR screen data analysis

Sequencing reads were mapped to the sgRNA library using the read_count_CRISPR_guides.pl script available in the GitHub repository (https://github.com/whitehead/barc/tree/main/Perl). The differential sgRNA abundance between DFMO-treated and untreated samples was identified using the Robust Rank Aggregation (RRA) algorithm implemented in the "test" command of MAGeCK (v0.5.9.3)[35].

Cell viability assays

K562, NOMO, HEL, and MEL cells were seeded in 6-well plates at defined densities and pre-treated with sardomozide. For 72-hour pre-treatment, 1×10^5 cells per well were plated in 1 mL of complete growth medium. For extended 96-hour pre-treatment, K562 cells were seeded at 2×10^5 cells per well in 1 mL of medium and passaged into fresh sardomozide-containing medium after 48 hours. Following completion of the pre-treatment period, cells were transferred to medium supplemented with either ML162 or RSL3 and incubated for an additional 24 to 48 hours prior to downstream viability assessment.

Lentivirus preparation and transduction

Lentiviral particles were produced by transient transfection of HEK293T cells with 2 µg of lentiviral transfer plasmid, 1 µg of packaging plasmid psPAX2, and 0.5 µg of envelope plasmid pCMV-VSV-G, using 8 µL of Lipofectamine LTX (Invitrogen, 15338-100) in 500 µL Opti-MEM Reduced Serum Medium (Gibco, 31985-070) according to the manufacturer's instructions. Viral supernatants were harvested 48 hours post-transfection, clarified by filtration through a 0.45-µm filter, and used to transduce target cells in the presence of 10 µg/mL polybrene (Millipore Sigma, TR1003G). Single guide RNA (sgRNA) sequences, Cas9 expression systems, and vector constructs used for CRISPR-Cas9 knockout are detailed in Table S2. Following antibiotic or fluorescence selection, single-cell clones were isolated, expanded, and validated for gene knockout by immunoblot analysis. Constructs used for the expression of iron and polyamine sensors are also listed in Table S2.

Western blot

Cells were washed with ice-cold PBS and lysed in RIPA lysis buffer (25 mM Tris-HCl pH 7.5 (Invitrogen 15567027), 150 mM NaCl (Invitrogen AM9760G), 1% (v/v) NP-40 (Fisher Scientific AAJ19628AP), 1% (w/v) sodium deoxycholate (Sigma-Aldrich D6750), 0.1% (w/v) SDS (Bio-Rad 1610302)) supplemented with 1% (v/v) HALT protease and phosphatase inhibitors (Thermo Scientific 78429) and 125 U/mL Benzonase nuclease (EMD Millipore E1014). Lysates were homogenized and incubated on ice for 30 min with intermittent vortexing every 10 min. Insoluble debris was removed by centrifugation at 21000× g for 10 min at 4°C. Clarified lysates were mixed with 4× Bolt lithium dodecyl sulfate (LDS) sample buffer (Invitrogen B0007) supplemented with 100 mM DTT (Thermo Scientific R0861) and heated at 70°C for 5 min. This boiling step was skipped for membrane proteins (TFRC, FSP1 and SLC40A1) and instead lysate was kept at 37°C for 30 min. Samples were resolved on a Bolt 4-12% Bis-tris polyacrylamide gel (Invitrogen, NW04122) and transferred to PVDF membranes (Invitrogen IB24002) using the iBlot 2 dry blotting system (Invitrogen IB21001).

Membranes were blocked for 1 h at room temperature in 5% (w/v) nonfat dry skim milk (BD Biosciences 232100) prepared in TBST (tris-buffered saline (Fisher Scientific AAJ60764K3) containing 0.1% (v/v) Tween-20 (Fisher Scientific BP337). Primary antibodies were diluted in 5% (w/v) BSA in TBST and incubated overnight at 4°C. After four washes in TBST, membranes were incubated with HRP-conjugated secondary antibodies diluted in 1% (w/v) skim milk in TBST for 1 hour at room temperature. Following four additional TBST washes, chemiluminescent signals were developed using SuperSignal West Femto Maximum Sensitivity Substrate (Thermo Scientific, 34095) and imaged with a ChemiDoc XRS+ system (Bio-Rad). Antibodies were used at the following dilutions: SRM (Proteintech,

19858-1-AP; 1:1000), SMS (Abcam, ab156879; 1:1000), β-actin (Abcam, ab20272; 1:50,000), ACSL4 (Thermo Fisher, PA5-27137; 1:5000), GPX4 (Abcam, ab41787; 1:2000), FSP1 (Cell Signaling Technology, 24972S; 1:1000), Hypusine (Millipore, ABS1064-I; 1:2500), FTH (Abcam, ab75973; 1:2000), TFRC (Invitrogen, 13-6800; 1:5000), SLC40A1 (Novus Biologicals, NBP1-21502; 1:2000), EGFP (Abcam, AB6556; 1:6000), and anti-rabbit HRP-conjugated secondary antibody (Sigma, A0545; 1:5000).

BODIPY staining

Cells were pre-treated with sardomozide for 96 h. ML162 was added 2.5 h prior to analysis. 400,000 cells per well were seeded on 6-well dishes for each treatment condition. Cells were incubated with C11-BODIPY (581/591) (5 μM) for 30 min at 37°C. Subsequently, cells were washed once in HBSS (Gibco) and then resuspended in 300 μL of fresh HBSS (Gibco) strained through a 35 μm cell strainer (Falcon tube with cell strainer cap) and analyzed using the FITC and PE-Texas Red filter. At least 10,000 events were analyzed per sample. Data was analyzed using FlowJo Software.

FENIX assay

Liposomes were prepared based on methods previously described[43]. Briefly, soy L-α-phosphatidylcholine (PC, Avanti) in chloroform was formed into a thin film using a rotary evaporator (Buchi). The film was hydrated in 3 mL of PBS and sonicated at for 3-5 minutes at 65°C to yield a 20 mM lipid solution. The sample then underwent 3 cycles of freeze-thawing followed by extrusion (Avestin Liposofast LF-50) once at 65°C through a 200 nm membrane (Cytiva Nuclepore) then 3X through 100 nm membranes (Cytiva Nuclepore). The lipid suspension was stored at 4°C. The experiment was performed as previously described[50]. In brief, 0.1 mM liposome was mixed with 2 μM STY-BODIPY (Cayman) and 275 μl of the mixture was added to a black 96-well plate, and compounds (putrescine, spermine or PMC) were added to the indicated concentration, and the samples were incubated for 30 min at 37 °C and initiated by 5 μl of 12 mM DTUN (Cayman) in ethanol, and mixed using pipette to start autoxidation. Data were acquired by STY-BODIPY excitation at 488 nm and emission was measured at 518 nm using a microplate reader.

ROS measurement

Cells were pre-treated with sardomozide (72 h) and tert-butyl hydroperoxide (3 h). Post-treatment, 1×10^6 cells per well were seeded into 6-well plates containing 2 mL of Hank's Balanced Salt Solution

(HBSS) per well. Sardomozide was reintroduced to maintain consistent treatment conditions. Cells were incubated with CM-H2DCFDA (2 μM) for 30 min at 37°C (dark). Following incubation, cells were resuspended in fresh RPMI 1640 medium (Gibco). Sardomozide and tBHP were added back to the cells to sustain treatment conditions. Flow cytometric analysis was performed using a FITC (505 nm, 530/30 nm) filter set. A minimum of 5,000 events were recorded per sample. Data were analyzed using FlowJo software.

RhoNoxM staining

Cells were pre-treated with sardomozide (72 h), washed twice with HBSS to remove extracellular iron, resuspended in IMDM, and counted. 0.5×10^6 cells/well were seeded into 6-well plates with 1 mL iron-free IMDM (Gibco); sardomozide was reintroduced. For iron detection, cells were incubated with RhoNox-M^{125} (2 μM, synthesized in-house) for 5 h at 37°C, with ferric ammonium sulfate added during the final hour. Cells were washed three times with pre-warmed HBSS and resuspended in IMDM. For lysosomal content, cells were stained with LysoTracker (20 nM, Thermo Fisher) for 30 min at 37°C in the dark and washed. Flow cytometry was performed using PE (570 nm, 580/14 nm) and APC (638 nm, 660/20 nm) channels. ≥5,000 events/sample were acquired and analyzed using FlowJo.

Iron measurements using ICP-MS

Cells were washed twice with HBSS, counted, and pelleted at 4×10^6 cells per experimental condition. Cell pellets were snap-frozen in liquid nitrogen and stored briefly at –80°C. For analysis, pellets were thawed and resuspended in 100 μL of trace metal–free water (VWR, 87003-236), transferred to metal-free perfluoroalkoxy (PFA) tubes, and lyophilized overnight. Dried pellets were resuspended in 100 μL of 67% trace metal–free nitric acid (VWR, 87003-226) and digested at 80°C for 20 hours. Digested samples were diluted with trace metal–free water to a final nitric acid concentration of 2%. Blank samples underwent identical processing. An Fe standard curve (0–100,000 ppb; Agilent, 5183-4688) was prepared, and a terbium internal standard (1 ppb final concentration; Agilent, 5190-8590) was added to all samples and standards. Total Fe was quantified using an Agilent 7900 inductively coupled plasma mass spectrometer (ICP-MS) operated with a helium collision cell to minimize polyatomic interferences. Data acquisition and quantification were performed using Agilent MassHunter Workstation software. Sample Fe concentrations were determined by interpolation from the standard curve, blank-subtracted, and normalized to cell number. Statistical analyses were conducted in GraphPad Prism.

Untargeted metabolomics

All tubes were pre-chilled, and steps were performed on ice unless otherwise noted. Cells were pelleted by centrifugation at 4°C, washed once with 1.5 mL of ice-cold 0.9% NaCl, and pelleted again to remove the wash solution. Cell pellets were immediately snap-frozen on dry ice. Cells were resuspended in 1 mL of 80% methanol (pre-chilled to 20°C). Tubes were vortexed for 10 minutes in a cold room. Samples were then dried using a SpeedVac concentrator. Dried extracts were stored at –80°C orior to LC-MS. Polar metabolites were analyzed using a QExactive Orbitrap MS (Thermo) with an Ion Max source and HESI II probe, coupled to a Dionex UltiMate 3000 UHPLC. External calibration was performed weekly. Samples (5 µL) were injected onto a SeQuant ZIC-pHILIC column (2.1 × 150 mm, 5 µm) with a matching guard column. Column and autosampler were maintained at 25°C and 4°C, respectively. Mobile phase A: 20 mM ammonium carbonate, 0.1% ammonium hydroxide; B: acetonitrile. Flow rate: 0.15 mL/min. Gradient: 0–20 min, 80–20% B; 20–20.5 min, 20–80% B; 20.5–28 min, 80% B hold. The MS operated in full-scan, polarity-switching mode (m/z 70–1000), 70,000 resolution, 3.0 kV spray voltage, 275°C capillary, 350°C HESI probe, sheath/aux/sweep gas: 40/15/1. AGC target was 1×10^6, max IT 20 ms. For untargeted metabolomics, $ddMS^2$ was acquired on pooled samples (Top 10 method, 15/30/45 V stepped collision energies, 17,500 resolution, AGC 2×10^5, max IT 100 ms, isolation window 1.0 m/z). Data were processed in Compound Discoverer 3.1 using an in-house mass list; P-values were Benjamini-Hochberg corrected.

Thiol metabolomics

Cysteine and GSH levels (Fig. S4C) were measured using a modified Ellman labeling protocol[126]. Briefly, 2×10^6 cells were pelleted, washed with ice-cold 0.9% NaCl, and extracted with 400 µL ice-cold 80% methanol. Internal standard (10 µL of 4.4 µM 13C,15N-cysteine; HY-Y03375) and 440 µL Ellman's reagent (10 mM in 80% methanol) were added. Samples were incubated on ice for 1 h, centrifuged (3,000 × g, 5 min), and supernatants stored at –80°C until analysis. Samples were run as above with a targeted selected ion monitoring scan (tSIM) in positive mode centred on m/z 319.00530 and m/z 323.01240 to increase signal for the cysteine-TNB (2-nitro-5-thiobenzoic acid) mixed disulfide and the [13C, 15N]cysteine–TNB mixed disulfide, respectively.

RNA-sequencing

Total RNA was extracted with PureLink RNA Mini Kit (Invitrogen) per the manufacturer's instruction. PolyA selection and RNA library construction were performed by Novogene with sequencing as 150 × 150 base paired-end libraries using an Illumina NovaSeq 6000 (Novogene), to a depth of ≥ 20M reads. Reads were aligned to the human genome (hg38, annotation file GRCh GTF 38.93) using the short-read alignment tool STAR (version 2.7.1a)[127] with the default options. Expression of each mRNA was calculated and reported as fragments per kilobase of transcript sequence per million base pairs sequenced (FPKM). The change in FPKM was compared between groups (e.g., control versus sardomozide) and differential expression was analyzed using the DESeq2 package. FDR correction was performed using the Benjamini-Hochberg method.

Enzymatic polyamine assay

Measurements were performed using the fluorescent quantification assays (abcam239728) as per the manufacturer's instructions. The polyamine assay buffer (no added polyamine standard) was used as the background.

C8-pos lipidomics

Cell pellets (4×10^6) were reconstituted in 1 mL isopropanol containing 1,2-didodecanoyl-sn-glycero-3-phosphocholine (Avanti) as internal standard, vortexed, and centrifuged (10,000 × g, 10 min). Supernatants (10 µL) were injected onto a 100 × 2.1 mm, 1.7 µm ACQUITY BEH C8 column (Waters). Lipidomic profiling was performed on a Shimadzu Nexera X2 U-HPLC coupled to an Exactive Plus Orbitrap MS (Thermo), operated in positive ion mode (full scan, m/z 220–1100, 70,000 resolution, 3 Hz acquisition). MS parameters: sheath gas 50, sweep gas 5, in-source CID 5 eV, spray voltage 3 kV, capillary/heater temperatures 300°C, S-lens RF 60, AGC target 1×10^6, max ion time 100 ms, 1 microscan. The column was eluted with 80% mobile phase A (95:5:0.1, 10 mM ammonium acetate/methanol/formic acid) for 1 min, ramped to 80% mobile phase B (99.9:0.1 methanol/formic acid) over 2 min, then to 100% B over 7 min, and held at 100% B for 3 min. Raw data were processed using TraceFinder software (Thermo Fisher Scientific) for targeted peak integration and manual review of a subset of identified lipids and using Progenesis QI (Nonlinear Dynamics) for peak detection and integration of both lipids of known identify and unknowns. Lipid identities were determined based on

comparison to reference plasma extracts and are denoted by total number of carbons in the lipid acyl chain(s) and total number of double bonds in the lipid acyl chain(s).

BODIPY 493/503 measurement

Cells were pre-treated with sardomozide (72 h) and oleic acid (18 h), then washed twice with HBSS to remove extracellular lipids. 0.5×10^6 cells/well were seeded into 6-well plates with 1 mL lipid-free IMDM, and sardomozide was reintroduced. Cells were incubated with BODIPY 493/503 (10 μM) for 1 h at 37°C, washed once with HBSS, and resuspended in RPMI 1640 (Gibco). Flow cytometry was performed using a FITC channel (excitation: 505 nm, emission: 530/30 nm), recording ≥5,000 events/sample. Data were analyzed with FlowJo.

References

1. Pegg, A.E. (2016). Functions of Polyamines in Mammals. J. Biol. Chem. *291*, 14904–14912. https://doi.org/10.1074/jbc.R116.731661.

2. Watanabe, S., Kusama-Eguchi, K., Kobayashi, H., and Igarashi, K. (1991). Estimation of polyamine binding to macromolecules and ATP in bovine lymphocytes and rat liver. J. Biol. Chem. *266*, 20803–20809.

3. Ghoda, L., van Daalen Wetters, T., Macrae, M., Ascherman, D., and Coffino, P. (1989). Prevention of rapid intracellular degradation of ODC by a carboxyl-terminal truncation. Science *243*, 1493–1495. https://doi.org/10.1126/science.2928784.

4. Coffino, P. (2001). Regulation of cellular polyamines by antizyme. Nat. Rev. Mol. Cell Biol. *2*, 188–194. https://doi.org/10.1038/35056508.

5. Pegg, A.E. (2008). Spermidine/spermine-N(1)-acetyltransferase: a key metabolic regulator. Am. J. Physiol. Endocrinol. Metab. *294*, E995-1010. https://doi.org/10.1152/ajpendo.90217.2008.

6. Murray Stewart, T., Dunston, T.T., Woster, P.M., and Casero, R.A. (2018). Polyamine catabolism and oxidative damage. J. Biol. Chem. *293*, 18736–18745. https://doi.org/10.1074/jbc.TM118.003337.

7. Park, M.H., and Wolff, E.C. (2018). Hypusine, a polyamine-derived amino acid critical for eukaryotic translation. J. Biol. Chem. *293*, 18710–18718. https://doi.org/10.1074/jbc.TM118.003341.

8. Park, S., Athreya, A., Carrizo, G.E., Benning, N.A., Mitchener, M.M., Bhanu, N.V., Garcia, B.A., Zhang, B., Muir, T.W., Pearce, E.L., et al. (2023). Electrostatic encoding of genome organization principles within single native nucleosomes. BioRxiv Prepr. Serv. Biol., 2023.12.08.570828. https://doi.org/10.1101/2023.12.08.570828.

9. Zhang, D., Zhao, T., Ang, H.S., Chong, P., Saiki, R., Igarashi, K., Yang, H., and Vardy, L.A. (2012). AMD1 is essential for ESC self-renewal and is translationally down-regulated on differentiation to neural precursor cells. Genes Dev. *26*, 461–473. https://doi.org/10.1101/gad.182998.111.

10. Minetti, A., Omrani, O., Brenner, C., Allies, G., Imada, S., Rösler, J., Khawaled, S., Cansiz, F., Meckelmann, S.W., Gebert, N., et al. (2024). Polyamines sustain epithelial regeneration in aged intestines by modulating protein homeostasis. Preprint at bioRxiv, https://doi.org/10.1101/2024.07.26.605278 https://doi.org/10.1101/2024.07.26.605278.

11. Hofer, S.J., Simon, A.K., Bergmann, M., Eisenberg, T., Kroemer, G., and Madeo, F. (2022). Mechanisms of spermidine-induced autophagy and geroprotection. Nat. Aging *2*, 1112–1129. https://doi.org/10.1038/s43587-022-00322-9.

12. Puleston, D.J., Baixauli, F., Sanin, D.E., Edwards-Hicks, J., Villa, M., Kabat, A.M., Kamiński, M.M., Stanckzak, M., Weiss, H.J., Grzes, K.M., et al. (2021). Polyamine metabolism is a central determinant of helper T cell lineage fidelity. Cell *184*, 4186-4202.e20. https://doi.org/10.1016/j.cell.2021.06.007.

13. Gupta, V.K., Scheunemann, L., Eisenberg, T., Mertel, S., Bhukel, A., Koemans, T.S., Kramer, J.M., Liu, K.S.Y., Schroeder, S., Stunnenberg, H.G., et al. (2013). Restoring polyamines protects from age-induced memory impairment in an autophagy-dependent manner. Nat. Neurosci. *16*, 1453–1460. https://doi.org/10.1038/nn.3512.

14. Eisenberg, T., Abdellatif, M., Schroeder, S., Primessnig, U., Stekovic, S., Pendl, T., Harger, A., Schipke, J., Zimmermann, A., Schmidt, A., et al. (2016). Cardioprotection and lifespan extension by the natural polyamine spermidine. Nat. Med. *22*, 1428–1438. https://doi.org/10.1038/nm.4222.

15. Eisenberg, T., Knauer, H., Schauer, A., Büttner, S., Ruckenstuhl, C., Carmona-Gutierrez, D., Ring, J., Schroeder, S., Magnes, C., Antonacci, L., et al. (2009). Induction of autophagy by spermidine promotes longevity. Nat. Cell Biol. *11*, 1305–1314. https://doi.org/10.1038/ncb1975.

16. Casero, R.A., Murray Stewart, T., and Pegg, A.E. (2018). Polyamine metabolism and cancer: treatments, challenges and opportunities. Nat. Rev. Cancer *18*, 681–695. https://doi.org/10.1038/s41568-018-0050-3.

17. van Veen, S., Martin, S., Van den Haute, C., Benoy, V., Lyons, J., Vanhoutte, R., Kahler, J.P., Decuypere, J.-P., Gelders, G., Lambie, E., et al. (2020). ATP13A2 deficiency disrupts lysosomal polyamine export. Nature *578*, 419–424. https://doi.org/10.1038/s41586-020-1968-7.

18. Schwartz, C.E., Wang, X., Stevenson, R.E., and Pegg, A.E. (2011). Spermine synthase deficiency resulting in X-linked intellectual disability (Snyder-Robinson syndrome). Methods Mol. Biol. Clifton NJ *720*, 437–445. https://doi.org/10.1007/978-1-61779-034-8_28.

19. Bachmann, A.S., VanSickle, E.A., Michael, J., Vipond, M., and Bupp, C.P. (2024). Bachmann-Bupp syndrome and treatment. Dev. Med. Child Neurol. *66*, 445–455. https://doi.org/10.1111/dmcn.15687.

20. Stewart, T.M., Foley, J.R., Holbert, C.E., Khomutov, M., Rastkari, N., Tao, X., Khomutov, A.R., Zhai, R.G., and Casero, R.A. (2023). Difluoromethylornithine rebalances aberrant polyamine ratios in Snyder-Robinson syndrome: mechanism of action and therapeutic potential. Preprint at bioRxiv, https://doi.org/10.1101/2023.03.30.534977 https://doi.org/10.1101/2023.03.30.534977.

21. Shalem, O., Sanjana, N.E., Hartenian, E., Shi, X., Scott, D.A., Mikkelson, T., Heckl, D., Ebert, B.L., Root, D.E., Doench, J.G., et al. (2014). Genome-scale CRISPR-Cas9 knockout screening in human cells. Science *343*, 84–87. https://doi.org/10.1126/science.1247005.

22. Wang, T., Wei, J.J., Sabatini, D.M., and Lander, E.S. (2014). Genetic screens in human cells using the CRISPR-Cas9 system. Science *343*, 80–84. https://doi.org/10.1126/science.1246981.

23. Yang, W.S., SriRamaratnam, R., Welsch, M.E., Shimada, K., Skouta, R., Viswanathan, V.S., Cheah, J.H., Clemons, P.A., Shamji, A.F., Clish, C.B., et al. (2014). Regulation of Ferroptotic Cancer Cell Death by GPX4. Cell *156*, 317–331. https://doi.org/10.1016/j.cell.2013.12.010.

24. Li, Z., Lange, M., Dixon, S.J., and Olzmann, J.A. (2024). Lipid Quality Control and Ferroptosis: From Concept to Mechanism. Annu. Rev. Biochem. *93*, 499–528. https://doi.org/10.1146/annurev-biochem-052521-033527.

25. Hares, G.B., Fernelius, W.C., and Douglas, B.E. (1956). Equilibrium Constants for the Formation of Complexes between Metal Ions and Polyamines1,2. J. Am. Chem. Soc. *78*, 1816–1818. https://doi.org/10.1021/ja01590a011.

26. Bertsch, C.R., Fernelius, W.C., and Block, B.P. (1958). A Thermodynamic Study of Some Complexes of Metal Ions with Polyamines. J. Phys. Chem. *62*, 444–450. https://doi.org/10.1021/j150562a018.

27. Palmer, B.N., and Powell, H.K.J. (1974). Complex formation between 4,9-diazadodecane-1,12-diamine (spermine) and copper(II) ions and protons in aqueous solution. J. Chem. Soc. Dalton Trans., 2086–2089. https://doi.org/10.1039/DT9740002086.

28. Voelter, W., Strobel, G.J., and Weser, U. (1975). Reaction of Cu++ with some polyamines of biochemical significance, a 13C-NMR study. Bioinorg. Chem. *5*, 183–188. https://doi.org/10.1016/s0006-3061(00)80059-9.

29. Barbucci, R., Campbell, M.J.M., Cannas, M., and Marongiu, G. (1980). Seven membered chelate rings in copper(II) complexes with spermidine. Inorganica Chim. Acta *46*, 135–138. https://doi.org/10.1016/S0020-1693(00)84181-X.

30. Templeton, D.M., and Sarkar, B. (1985). Fletcher–Powell minimization of analytical potentiometric data by microcomputer: application to the Cu(II) complexes of biological polyamines. Can. J. Chem. *63*, 3122–3128. https://doi.org/10.1139/v85-515.

31. Lomozik, L., Gasowska, A., Bregier-Jarzebowska, R., and Jastrzab, R. (2005). Coordination chemistry of polyamines and their interactions in ternary systems including metal ions, nucleosides and nucleotides. Coord. Chem. Rev. *249*, 2335–2350. https://doi.org/10.1016/j.ccr.2005.05.002.

32. Jastrzab, R., Kaczmarek, M.T., Nowak, M., Trojanowska, A., and Zabiszak, M. (2017). Complexes of polyamines and their derivatives as living system active compounds. Coord. Chem. Rev. *351*, 32–44. https://doi.org/10.1016/j.ccr.2017.05.001.

33. Park, S., Merino-Urteaga, R., Karwacki-Neisius, V., Carrizo, G.E., Athreya, A., Marin-Gonzalez, A., Benning, N.A., Park, J., Mitchener, M.M., Bhanu, N.V., et al. (2025). Native nucleosomes intrinsically encode genome organization principles. Nature. https://doi.org/10.1038/s41586-025-08971-7.

34. Inglis, A.J., Guna, A., Gálvez-Merchán, Á., Pal, A., Esantsi, T.K., Keys, H.R., Frenkel, E.M., Oania, R., Weissman, J.S., and Voorhees, R.M. (2023). Coupled protein quality control during nonsense-mediated mRNA decay. J. Cell Sci. *136*, jcs261216. https://doi.org/10.1242/jcs.261216.

35. Li, W., Xu, H., Xiao, T., Cong, L., Love, M.I., Zhang, F., Irizarry, R.A., Liu, J.S., Brown, M., and Liu, X.S. (2014). MAGeCK enables robust identification of essential genes from genome-scale CRISPR/Cas9 knockout screens. Genome Biol. *15*, 554. https://doi.org/10.1186/s13059-014-0554-4.

36. Uemura, T., Yerushalmi, H.F., Tsaprailis, G., Stringer, D.E., Pastorian, K.E., Hawel, L., Byus, C.V., and Gerner, E.W. (2008). Identification and Characterization of a Diamine Exporter in Colon Epithelial Cells. J. Biol. Chem. *283*, 26428–26435. https://doi.org/10.1074/jbc.M804714200.

37. Goldmann, U., and Sedlyarov, V. (2019). RESOLUTE database.

38. Hamouda, N.N., Van den Haute, C., Vanhoutte, R., Sannerud, R., Azfar, M., Mayer, R., Cortés Calabuig, Á., Swinnen, J.V., Agostinis, P., Baekelandt, V., et al. (2021). ATP13A3 is a major component of the enigmatic mammalian polyamine transport system. J. Biol. Chem. *296*, 100182. https://doi.org/10.1074/jbc.RA120.013908.

39. Vander Heiden, M.G., Li, X.X., Gottleib, E., Hill, R.B., Thompson, C.B., and Colombini, M. (2001). Bcl-xL promotes the open configuration of the voltage-dependent anion channel and metabolite passage through the outer mitochondrial membrane. J. Biol. Chem. *276*, 19414–19419. https://doi.org/10.1074/jbc.M101590200.

40. Bi, G., Liang, J., Bian, Y., Shan, G., Huang, Y., Lu, T., Zhang, H., Jin, X., Chen, Z., Zhao, M., et al. (2024). Polyamine-mediated ferroptosis amplification acts as a targetable vulnerability in cancer. Nat. Commun. *15*, 2461. https://doi.org/10.1038/s41467-024-46776-w.

41. Zilka, O., Shah, R., Li, B., Friedmann Angeli, J.P., Griesser, M., Conrad, M., and Pratt, D.A. (2017). On the Mechanism of Cytoprotection by Ferrostatin-1 and Liproxstatin-1 and the Role of Lipid Peroxidation in Ferroptotic Cell Death. ACS Cent. Sci. *3*, 232–243. https://doi.org/10.1021/acscentsci.7b00028.

42. Cañeque, T., Baron, L., Müller, S., Carmona, A., Colombeau, L., Versini, A., Solier, S., Gaillet, C., Sindikubwabo, F., Sampaio, J.L., et al. (2025). Activation of lysosomal iron triggers ferroptosis in cancer. Nature *642*, 492–500. https://doi.org/10.1038/s41586-025-08974-4.

43. Li, Y., Ran, Q., Duan, Q., Jin, J., Wang, Y., Yu, L., Wang, C., Zhu, Z., Chen, X., Weng, L., et al. (2024). 7-Dehydrocholesterol dictates ferroptosis sensitivity. Nature *626*, 411–418. https://doi.org/10.1038/s41586-023-06983-9.

44. Tsvetkov, P., Coy, S., Petrova, B., Dreishpoon, M., Verma, A., Abdusamad, M., Rossen, J., Joesch-Cohen, L., Humeidi, R., Spangler, R.D., et al. (2022). Copper induces cell death by targeting lipoylated TCA cycle proteins. Science *375*, 1254–1261. https://doi.org/10.1126/science.abf0529.

45. Alvarez, S.W., Sviderskiy, V.O., Terzi, E.M., Papagiannakopoulos, T., Moreira, A.L., Adams, S., Sabatini, D.M., Birsoy, K., and Possemato, R. (2017). NFS1 undergoes positive selection in lung tumours and protects cells from ferroptosis. Nature *551*, 639–643. https://doi.org/10.1038/nature24637.

46. Tada, K., Nishizawa, H., Shima, H., Muto, A., Wada, M., and Igarashi, K. (2024). Cysteine restriction induces ferroptosis depending on the polyamine biosynthetic pathway in hepatic cancer cells. Preprint at bioRxiv, https://doi.org/10.1101/2024.02.29.582667 https://doi.org/10.1101/2024.02.29.582667.

47. Sanayama, H., Ito, K., Ookawara, S., Uemura, T., Sakiyama, Y., Sugawara, H., Tabei, K., Igarashi, K., and Soda, K. (2023). Whole Blood Spermine/Spermidine Ratio as a New Indicator of Sarcopenia Status in Older Adults. Biomedicines *11*, 1403. https://doi.org/10.3390/biomedicines11051403.

48. Drolet, G., Dumbroff, E.B., Legge, R.L., and Thompson, J.E. (1986). Radical scavenging properties of polyamines. Phytochemistry *25*, 367–371. https://doi.org/10.1016/S0031-9422(00)85482-5.

49. Fujisawa, S., and Kadoma, Y. (2005). Kinetic evaluation of polyamines as radical scavengers. Anticancer Res. *25*, 965–969.

50. Shah, R., Farmer, L.A., Zilka, O., Van Kessel, A.T.M., and Pratt, D.A. (2019). Beyond DPPH: Use of Fluorescence-Enabled Inhibited Autoxidation to Predict Oxidative Cell Death Rescue. Cell Chem. Biol. *26*, 1594-1607.e7. https://doi.org/10.1016/j.chembiol.2019.09.007.

51. Ha, H.C., Sirisoma, N.S., Kuppusamy, P., Zweier, J.L., Woster, P.M., and Casero, R.A. (1998). The natural polyamine spermine functions directly as a free radical scavenger. Proc. Natl. Acad. Sci. U. S. A. *95*, 11140–11145. https://doi.org/10.1073/pnas.95.19.11140.

52. Oparka, M., Walczak, J., Malinska, D., van Oppen, L.M.P.E., Szczepanowska, J., Koopman, W.J.H., and Wieckowski, M.R. (2016). Quantifying ROS levels using CM-H2DCFDA and HyPer. Methods San Diego Calif *109*, 3–11. https://doi.org/10.1016/j.ymeth.2016.06.008.

53. Ma, Q. (2013). Role of nrf2 in oxidative stress and toxicity. Annu. Rev. Pharmacol. Toxicol. *53*, 401–426. https://doi.org/10.1146/annurev-pharmtox-011112-140320.

54. Doll, S., Proneth, B., Tyurina, Y.Y., Panzilius, E., Kobayashi, S., Ingold, I., Irmler, M., Beckers, J., Aichler, M., Walch, A., et al. (2017). ACSL4 dictates ferroptosis sensitivity by shaping cellular lipid composition. Nat. Chem. Biol. *13*, 91–98. https://doi.org/10.1038/nchembio.2239.

55. Doll, S., Freitas, F.P., Shah, R., Aldrovandi, M., da Silva, M.C., Ingold, I., Goya Grocin, A., Xavier da Silva, T.N., Panzilius, E., Scheel, C.H., et al. (2019). FSP1 is a glutathione-independent ferroptosis suppressor. Nature *575*, 693–698. https://doi.org/10.1038/s41586-019-1707-0.

56. Bersuker, K., Hendricks, J.M., Li, Z., Magtanong, L., Ford, B., Tang, P.H., Roberts, M.A., Tong, B., Maimone, T.J., Zoncu, R., et al. (2019). The CoQ oxidoreductase FSP1 acts parallel to GPX4 to inhibit ferroptosis. Nature *575*, 688–692. https://doi.org/10.1038/s41586-019-1705-2.

57. Schuller, A.P., Wu, C.C.-C., Dever, T.E., Buskirk, A.R., and Green, R. (2017). eIF5A Functions Globally in Translation Elongation and Termination. Mol. Cell *66*, 194-205.e5. https://doi.org/10.1016/j.molcel.2017.03.003.

58. Manjunath, H., Zhang, H., Rehfeld, F., Han, J., Chang, T.-C., and Mendell, J.T. (2019). Suppression of Ribosomal Pausing by eIF5A Is Necessary to Maintain the Fidelity of Start Codon Selection. Cell Rep. *29*, 3134-3146.e6. https://doi.org/10.1016/j.celrep.2019.10.129.

59. Rodencal, J., Kim, N., He, A., Li, V.L., Lange, M., He, J., Tarangelo, A., Schafer, Z.T., Olzmann, J.A., Long, J.Z., et al. (2024). Sensitization of cancer cells to ferroptosis coincident with cell cycle arrest. Cell Chem. Biol. *31*, 234-248.e13. https://doi.org/10.1016/j.chembiol.2023.10.011.

60. Ou, Y., Wang, S.-J., Li, D., Chu, B., and Gu, W. (2016). Activation of SAT1 engages polyamine metabolism with p53-mediated ferroptotic responses. Proc. Natl. Acad. Sci. *113*, E6806–E6812. https://doi.org/10.1073/pnas.1607152113.

61. Boggs, R., and Donohue, J. (1975). Spermine copper(II) perchlorate. Acta Crystallogr. B *31*, 320–322. https://doi.org/10.1107/S0567740875002658.

62. LØVaas, E. (1996). Antioxidative and Metal-Chelating Effects of Polyamines11Dedicated to the memory of David E. Green: Long gone but not forgotten. In Advances in Pharmacology, H. Sies, ed. (Academic Press), pp. 119–149. https://doi.org/10.1016/S1054-3589(08)60982-5.

63. Kontoghiorghes, G.J., and Kontoghiorghe, C.N. (2020). Iron and Chelation in Biochemistry and Medicine: New Approaches to Controlling Iron Metabolism and Treating Related Diseases. Cells *9*, 1456. https://doi.org/10.3390/cells9061456.

64. Zhang, Y., Zhao, X., Qin, Y., Li, X., Chang, Y., Shi, Z., Song, M., Sun, W., Xiao, J., Li, Z., et al. (2023). Order-order assembly transition-driven polyamines detection based on iron-sulfur complexes. Commun. Chem. *6*, 146. https://doi.org/10.1038/s42004-023-00942-1.

65. Lomozik, L., and Jastrzab, R. (2003). Copper(II) complexes with uridine, uridine 5'-monophosphate, spermidine, or spermine in aqueous solution. J. Inorg. Biochem. *93*, 132–140. https://doi.org/10.1016/s0162-0134(02)00567-6.

66. Tadolini, B. (1988). The influence of polyamine-nucleic acid complexes on Fe2+ autoxidation. Mol. Cell. Biochem. *83*, 179–185. https://doi.org/10.1007/BF00226145.

67. Kumar, V., Mishra, R.K., Ghose, D., Kalita, A., Dhiman, P., Prakash, A., Thakur, N., Mitra, G., Chaudhari, V.D., Arora, A., et al. (2022). Free spermidine evokes superoxide radicals that manifest toxicity. eLife *11*, e77704. https://doi.org/10.7554/eLife.77704.

68. Kitada, M., Igarashi, K., Hirose, S., and Kitagawa, H. (1979). Inhibition by polyamines of lipid peroxide formation in rat liver microsomes. Biochem. Biophys. Res. Commun. *87*, 388–394. https://doi.org/10.1016/0006-291x(79)91808-4.

69. Tadolini, B., Cabrini, L., Landi, L., Varani, E., and Pasquali, P. (1984). Polyamine binding to phospholipid vesicles and inhibition of lipid peroxidation. Biochem. Biophys. Res. Commun. *122*, 550–555. https://doi.org/10.1016/s0006-291x(84)80068-6.

70. Kamlin, C.O.F., M. Jenkins, T., L Heise, J., and S. Amin, N. (2024). Trientine Tetrahydrochloride, From Bench to Bedside: A Narrative Review. Drugs *84*, 1509–1518. https://doi.org/10.1007/s40265-024-02099-0.

71. Roberts, E.A., Schilsky, M.L., and American Association for Study of Liver Diseases (AASLD) (2008). Diagnosis and treatment of Wilson disease: an update. Hepatol. Baltim. Md *47*, 2089–2111. https://doi.org/10.1002/hep.22261.

72. Perry, A.R., Pagliuca, A., Fitzsimons, E.J., Mufti, G.J., and Williams, R. (1996). Acquired sideroblastic anaemia induced by a copper-chelating agent. Int. J. Hematol. *64*, 69–72. https://doi.org/10.1016/0925-5710(96)00457-4.

73. Lane, D.J.R., Bae, D.-H., Siafakas, A.R., Suryo Rahmanto, Y., Al-Akra, L., Jansson, P.J., Casero, R.A., and Richardson, D.R. (2018). Coupling of the polyamine and iron metabolism pathways in the regulation of proliferation: Mechanistic links to alterations in key polyamine biosynthetic and catabolic enzymes. Biochim. Biophys. Acta Mol. Basis Dis. *1864*, 2793–2813. https://doi.org/10.1016/j.bbadis.2018.05.007.

74. Tangella, A.V., Gajre, A.S., Chirumamilla, P.C., and Rathhan, P.V. Difluoromethylornithine (DFMO) and Neuroblastoma: A Review. Cureus *15*, e37680. https://doi.org/10.7759/cureus.37680.

75. Ramirez, A., Heimbach, A., Gründemann, J., Stiller, B., Hampshire, D., Cid, L.P., Goebel, I., Mubaidin, A.F., Wriekat, A.-L., Roeper, J., et al. (2006). Hereditary parkinsonism with dementia is caused by mutations in ATP13A2, encoding a lysosomal type 5 P-type ATPase. Nat. Genet. *38*, 1184–1191. https://doi.org/10.1038/ng1884.

76. Kırımtay, K., Temizci, B., Gültekin, M., Yapıcı, Z., and Karabay, A. (2021). Novel mutations in ATP13A2 associated with mixed neurological presentations and iron toxicity due to nonsense-mediated decay. Brain Res. *1750*, 147167. https://doi.org/10.1016/j.brainres.2020.147167.

77. Schneider, S.A., Paisan-Ruiz, C., Quinn, N.P., Lees, A.J., Houlden, H., Hardy, J., and Bhatia, K.P. (2010). ATP13A2 mutations (PARK9) cause neurodegeneration with brain iron accumulation. Mov. Disord. *25*, 979–984. https://doi.org/10.1002/mds.22947.

78. Rajagopalan, S., Rane, A., Chinta, S.J., and Andersen, J.K. (2016). Regulation of ATP13A2 via PHD2-HIF1α Signaling Is Critical for Cellular Iron Homeostasis: Implications for Parkinson's

Disease. J. Neurosci. Off. J. Soc. Neurosci. *36*, 1086–1095. https://doi.org/10.1523/JNEUROSCI.3117-15.2016.

79. Gitler, A.D., Chesi, A., Geddie, M.L., Strathearn, K.E., Hamamichi, S., Hill, K.J., Caldwell, K.A., Caldwell, G.A., Cooper, A.A., Rochet, J.-C., et al. (2009). Alpha-synuclein is part of a diverse and highly conserved interaction network that includes PARK9 and manganese toxicity. Nat. Genet. *41*, 308–315. https://doi.org/10.1038/ng.300.

80. Schmidt, K., Wolfe, D.M., Stiller, B., and Pearce, D.A. (2009). Cd2+, Mn2+, Ni2+ and Se2+ toxicity to *Saccharomyces cerevisiae* lacking YPK9p the orthologue of human ATP13A2. Biochem. Biophys. Res. Commun. *383*, 198–202. https://doi.org/10.1016/j.bbrc.2009.03.151.

81. Kong, S.M.Y., Chan, B.K.K., Park, J.-S., Hill, K.J., Aitken, J.B., Cottle, L., Farghaian, H., Cole, A.R., Lay, P.A., Sue, C.M., et al. (2014). Parkinson's disease-linked human PARK9/ATP13A2 maintains zinc homeostasis and promotes α-Synuclein externalization via exosomes. Hum. Mol. Genet. *23*, 2816–2833. https://doi.org/10.1093/hmg/ddu099.

82. Rinaldi, D.E., Corradi, G.R., Cuesta, L.M., Adamo, H.P., and de Tezanos Pinto, F. (2015). The Parkinson-associated human P5B-ATPase ATP13A2 protects against the iron-induced cytotoxicity. Biochim. Biophys. Acta *1848*, 1646–1655. https://doi.org/10.1016/j.bbamem.2015.04.008.

83. Martin, S., van Veen, S., Holemans, T., Demirsoy, S., van den Haute, C., Baekelandt, V., Agostinis, P., Eggermont, J., and Vangheluwe, P. (2016). Protection against Mitochondrial and Metal Toxicity Depends on Functional Lipid Binding Sites in ATP13A2. Park. Dis. *2016*, e9531917. https://doi.org/10.1155/2016/9531917.

84. Sharma, P., Kim, C.Y., Keys, H.R., Imada, S., Joseph, A.B., Ferro, L., Kunchok, T., Anderson, R., Yilmaz, O., Weng, J.-K., et al. (2024). Genetically encoded fluorescent reporter for polyamines. BioRxiv Prepr. Serv. Biol., 2024.08.24.609500. https://doi.org/10.1101/2024.08.24.609500.

85. Liu, B., Azfar, M., Legchenko, E., West, J.A., Martin, S., Van den Haute, C., Baekelandt, V., Wharton, J., Howard, L., Wilkins, M.R., et al. (2024). ATP13A3 variants promote pulmonary arterial hypertension by disrupting polyamine transport. Cardiovasc. Res. *120*, 756–768. https://doi.org/10.1093/cvr/cvae068.

86. Soon, E., Treacy, C.M., Toshner, M.R., MacKenzie-Ross, R., Manglam, V., Busbridge, M., Sinclair-McGarvie, M., Arnold, J., Sheares, K.K., Morrell, N.W., et al. (2011). Unexplained iron deficiency in idiopathic and heritable pulmonary arterial hypertension. Thorax *66*, 326–332. https://doi.org/10.1136/thx.2010.147272.

87. Galy, B., Conrad, M., and Muckenthaler, M. (2023). Mechanisms controlling cellular and systemic iron homeostasis. Nat. Rev. Mol. Cell Biol., 1–23. https://doi.org/10.1038/s41580-023-00648-1.

88. Plays, M., Müller, S., and Rodriguez, R. (2021). Chemistry and biology of ferritin. Met. Integr. Biometal Sci. *13*, mfab021. https://doi.org/10.1093/mtomcs/mfab021.

89. Brawley, H.N., Kreinbrink, A.C., Hierholzer, J.D., Vali, S.W., and Lindahl, P.A. (2023). Labile Iron Pool of Isolated Escherichia coli Cytosol Likely Includes Fe-ATP and Fe-Citrate but not Fe-

Glutathione or Aqueous Fe. J. Am. Chem. Soc. *145*, 2104–2117. https://doi.org/10.1021/jacs.2c06625.

90. Cancer Genome Atlas Network (2012). Comprehensive molecular characterization of human colon and rectal cancer. Nature *487*, 330–337. https://doi.org/10.1038/nature11252.

91. Goto, N., Westcott, P.M.K., Goto, S., Imada, S., Taylor, M.S., Eng, G., Braverman, J., Deshpande, V., Jacks, T., Agudo, J., et al. (2024). SOX17 enables immune evasion of early colorectal adenomas and cancers. Nature *627*, 636–645. https://doi.org/10.1038/s41586-024-07135-3.

92. Hentze, M.W., Muckenthaler, M.U., and Andrews, N.C. (2004). Balancing acts: molecular control of mammalian iron metabolism. Cell *117*, 285–297. https://doi.org/10.1016/s0092-8674(04)00343-5.

93. Tang, Z., Li, C., Kang, B., Gao, G., Li, C., and Zhang, Z. (2017). GEPIA: a web server for cancer and normal gene expression profiling and interactive analyses. Nucleic Acids Res. *45*, W98–W102. https://doi.org/10.1093/nar/gkx247.

94. Bello-Fernandez, C., Packham, G., and Cleveland, J.L. (1993). The ornithine decarboxylase gene is a transcriptional target of c-Myc. Proc. Natl. Acad. Sci. U. S. A. *90*, 7804–7808. https://doi.org/10.1073/pnas.90.16.7804.

95. Origanti, S., and Shantz, L.M. (2007). Ras transformation of RIE-1 cells activates cap-independent translation of ornithine decarboxylase: regulation by the Raf/MEK/ERK and phosphatidylinositol 3-kinase pathways. Cancer Res. *67*, 4834–4842. https://doi.org/10.1158/0008-5472.CAN-06-4627.

96. Roy, U.K.B., Rial, N.S., Kachel, K.L., and Gerner, E.W. (2008). Activated K-RAS increases polyamine uptake in human colon cancer cells through modulation of caveolar endocytosis. Mol. Carcinog. *47*, 538–553. https://doi.org/10.1002/mc.20414.

97. Kucharzewska, P., Welch, J.E., Svensson, K.J., and Belting, M. (2009). The polyamines regulate endothelial cell survival during hypoxic stress through PI3K/AKT and MCL-1. Biochem. Biophys. Res. Commun. *380*, 413–418. https://doi.org/10.1016/j.bbrc.2009.01.097.

98. Zabala-Letona, A., Arruabarrena-Aristorena, A., Martín-Martín, N., Fernandez-Ruiz, S., Sutherland, J.D., Clasquin, M., Tomas-Cortazar, J., Jimenez, J., Torres, I., Quang, P., et al. (2017). mTORC1-dependent AMD1 regulation sustains polyamine metabolism in prostate cancer. Nature *547*, 109–113. https://doi.org/10.1038/nature22964.

99. Hogarty, M.D., Norris, M.D., Davis, K., Liu, X., Evageliou, N.F., Hayes, C.S., Pawel, B., Guo, R., Zhao, H., Sekyere, E., et al. (2008). ODC1 is a critical determinant of MYCN oncogenesis and a therapeutic target in neuroblastoma. Cancer Res. *68*, 9735–9745. https://doi.org/10.1158/0008-5472.CAN-07-6866.

100. Rounbehler, R.J., Li, W., Hall, M.A., Yang, C., Fallahi, M., and Cleveland, J.L. (2009). Targeting ornithine decarboxylase impairs development of MYCN-amplified neuroblastoma. Cancer Res. *69*, 547–553. https://doi.org/10.1158/0008-5472.CAN-08-2968.

101. Manni, A., Washington, S., Hu, X., Griffith, J.W., Bruggeman, R., Demers, L.M., Mauger, D., and Verderame, M.F. (2005). Effects of polyamine synthesis inhibitors on primary tumor features and metastatic capacity of human breast cancer cells. Clin. Exp. Metastasis *22*, 255–263. https://doi.org/10.1007/s10585-005-8480-1.

102. Klein, S., Miret, J.J., Algranati, I.D., and de Lustig, E.S. (1985). Effect of alpha-difluoromethylornithine in lung metastases before and after surgery of primary adenocarcinoma tumors in mice. Biol. Cell *53*, 33–36. https://doi.org/10.1111/j.1768-322x.1985.tb00352.x.

103. Herr, H.W., Kleinert, E.L., Conti, P.S., Burchenal, J.H., and Whitmore, W.F. (1984). Effects of alpha-difluoromethylornithine and methylglyoxal bis(guanylhydrazone) on the growth of experimental renal adenocarcinoma in mice. Cancer Res. *44*, 4382–4385.

104. Kubota, S., Ohsawa, N., and Takaku, F. (1987). Effects of DL-alpha-difluoromethylornithine on the growth and metastasis of B16 melanoma in vivo. Int. J. Cancer *39*, 244–247. https://doi.org/10.1002/ijc.2910390220.

105. Kubota, S., Kiyosawa, H., Nomura, Y., Yamada, T., and Seyama, Y. (1997). Ornithine decarboxylase overexpression in mouse 10T1/2 fibroblasts: cellular transformation and invasion. J. Natl. Cancer Inst. *89*, 567–571. https://doi.org/10.1093/jnci/89.8.567.

106. Hibino, S., Eto, S., Hangai, S., Endo, K., Ashitani, S., Sugaya, M., Osawa, T., Soga, T., Taniguchi, T., and Yanai, H. (2023). Tumor cell-derived spermidine is an oncometabolite that suppresses TCR clustering for intratumoral CD8+ T cell activation. Proc. Natl. Acad. Sci. U. S. A. *120*, e2305245120. https://doi.org/10.1073/pnas.2305245120.

107. Sholler, G.L.S., Ferguson, W., Bergendahl, G., Bond, J.P., Neville, K., Eslin, D., Brown, V., Roberts, W., Wada, R.K., Oesterheld, J., et al. (2018). Maintenance DFMO Increases Survival in High Risk Neuroblastoma. Sci. Rep. *8*, 14445. https://doi.org/10.1038/s41598-018-32659-w.

108. Simoneau, A.R., Gerner, E.W., Nagle, R., Ziogas, A., Fujikawa-Brooks, S., Yerushalmi, H., Ahlering, T.E., Lieberman, R., McLaren, C.E., Anton-Culver, H., et al. (2008). The Effect of Difluoromethylornithine on Decreasing Prostate Size and Polyamines in Men: Results of a Year-Long Phase IIb Randomized Placebo-Controlled Chemoprevention Trial. Cancer Epidemiol. Biomark. Prev. Publ. Am. Assoc. Cancer Res. Cosponsored Am. Soc. Prev. Oncol. *17*, 292–299. https://doi.org/10.1158/1055-9965.EPI-07-0658.

109. Holbert, C.E., Cullen, M.T., Casero, R.A., and Stewart, T.M. (2022). Polyamines in cancer: integrating organismal metabolism and antitumour immunity. Nat. Rev. Cancer *22*, 467–480. https://doi.org/10.1038/s41568-022-00473-2.

110. Offenbacher, R., Jackson, K.W., Hayashi, M., Zhang, J., Peng, D., Tan, Y., Stewart, T.M., Ciero, P., Foley, J., Casero, R.A., et al. (2024). Polyamine Depletion by D, L-alpha-difluoromethylornithine Inhibits Ewing Sarcoma Metastasis by Inducing Ferroptosis. BioRxiv Prepr. Serv. Biol., 2024.06.14.599064. https://doi.org/10.1101/2024.06.14.599064.

111. Lam, B., Kajderowicz, K.M., Keys, H.R., Roessler, J.M., Frenkel, E.M., Kirkland, A., Bisht, P., El-Brolosy, M.A., Jaenisch, R., Bell, G.W., et al. (2024). Multi-species genome-wide CRISPR

screens identify conserved suppressors of cold-induced cell death. BioRxiv Prepr. Serv. Biol., 2024.07.25.605098. https://doi.org/10.1101/2024.07.25.605098.

112. Mazhar, M., Din, A.U., Ali, H., Yang, G., Ren, W., Wang, L., Fan, X., and Yang, S. (2021). Implication of ferroptosis in aging. Cell Death Discov. *7*, 149. https://doi.org/10.1038/s41420-021-00553-6.

113. Zhuang, X., Wang, Q., Joost, S., Ferrena, A., Humphreys, D.T., Li, Z., Blum, M., Krause, K., Ding, S., Landais, Y., et al. (2025). Ageing limits stemness and tumorigenesis by reprogramming iron homeostasis. Nature *637*, 184–194. https://doi.org/10.1038/s41586-024-08285-0.

114. Tamari, K., Konno, M., Asai, A., Koseki, J., Hayashi, K., Kawamoto, K., Murai, N., Matsufuji, S., Isohashi, F., Satoh, T., et al. (2018). Polyamine flux suppresses histone lysine demethylases and enhances ID1 expression in cancer stem cells. Cell Death Discov. *4*, 104. https://doi.org/10.1038/s41420-018-0117-7.

115. Müller, S., Sindikubwabo, F., Cañeque, T., Lafon, A., Versini, A., Lombard, B., Loew, D., Wu, T.-D., Ginestier, C., Charafe-Jauffret, E., et al. (2020). CD44 regulates epigenetic plasticity by mediating iron endocytosis. Nat. Chem. *12*, 929–938. https://doi.org/10.1038/s41557-020-0513-5.

116. Mai, T.T., Hamaï, A., Hienzsch, A., Cañeque, T., Müller, S., Wicinski, J., Cabaud, O., Leroy, C., David, A., Acevedo, V., et al. (2017). Salinomycin kills cancer stem cells by sequestering iron in lysosomes. Nat. Chem. *9*, 1025–1033. https://doi.org/10.1038/nchem.2778.

117. Schonberg, D.L., Miller, T.E., Wu, Q., Flavahan, W.A., Das, N.K., Hale, J.S., Hubert, C.G., Mack, S.C., Jarrar, A.M., Karl, R.T., et al. (2015). Preferential Iron Trafficking Characterizes Glioblastoma Stem-like Cells. Cancer Cell *28*, 441–455. https://doi.org/10.1016/j.ccell.2015.09.002.

118. Badgley, M.A., Kremer, D.M., Maurer, H.C., DelGiorno, K.E., Lee, H.-J., Purohit, V., Sagalovskiy, I.R., Ma, A., Kapilian, J., Firl, C.E.M., et al. (2020). Cysteine depletion induces pancreatic tumor ferroptosis in mice. Science *368*, 85–89. https://doi.org/10.1126/science.aaw9872.

119. Ezeriņa, D., Takano, Y., Hanaoka, K., Urano, Y., and Dick, T.P. (2018). N-Acetyl Cysteine Functions as a Fast-Acting Antioxidant by Triggering Intracellular H2S and Sulfane Sulfur Production. Cell Chem. Biol. *25*, 447-459.e4. https://doi.org/10.1016/j.chembiol.2018.01.011.

120. Cruz-Pulido, Y.E., LoMascolo, N.J., May, D., Hatahet, J., Thomas, C.E., Chu, A.K.W., Stacey, S.P., Villanueva Guzman, M. del M., Aubert, G., and Mounce, B.C. (2024). Polyamines mediate cellular energetics and lipid metabolism through mitochondrial respiration to facilitate virus replication. PLOS Pathog. *20*, e1012711. https://doi.org/10.1371/journal.ppat.1012711.

121. Zou, Y., Henry, W.S., Ricq, E.L., Graham, E.T., Phadnis, V.V., Maretich, P., Paradkar, S., Boehnke, N., Deik, A.A., Reinhardt, F., et al. (2020). Plasticity of ether lipids promotes ferroptosis susceptibility and evasion. Nature *585*, 603–608. https://doi.org/10.1038/s41586-020-2732-8.

122. Dixon, S.J., and Olzmann, J.A. (2024). The cell biology of ferroptosis. Nat. Rev. Mol. Cell Biol. *25*, 424–442. https://doi.org/10.1038/s41580-024-00703-5.

123. Cordella-Miele, E., Miele, L., Beninati, S., and Mukherjee, A.B. (1993). Transglutaminase-Catalyzed Incorporation of Polyamines into Phospholipase A2. J. Biochem. (Tokyo) *113*, 164–173. https://doi.org/10.1093/oxfordjournals.jbchem.a124021.

124. Stewart, S.A., Dykxhoorn, D.M., Palliser, D., Mizuno, H., Yu, E.Y., An, D.S., Sabatini, D.M., Chen, I.S.Y., Hahn, W.C., Sharp, P.A., et al. (2003). Lentivirus-delivered stable gene silencing by RNAi in primary cells. RNA N. Y. N *9*, 493–501. https://doi.org/10.1261/rna.2192803.

125. Niwa, M., Hirayama, T., Okuda, K., and Nagasawa, H. (2014). A new class of high-contrast Fe(II) selective fluorescent probes based on spirocyclized scaffolds for visualization of intracellular labile iron delivered by transferrin. Org. Biomol. Chem. *12*, 6590–6597. https://doi.org/10.1039/C4OB00935E.

126. Adelmann, C.H., Traunbauer, A.K., Chen, B., Condon, K.J., Chan, S.H., Kunchok, T., Lewis, C.A., and Sabatini, D.M. (2020). MFSD12 mediates the import of cysteine into melanosomes and lysosomes. Nature *588*, 699–704. https://doi.org/10.1038/s41586-020-2937-x.

127. Dobin, A., Davis, C.A., Schlesinger, F., Drenkow, J., Zaleski, C., Jha, S., Batut, P., Chaisson, M., and Gingeras, T.R. (2013). STAR: ultrafast universal RNA-seq aligner. Bioinforma. Oxf. Engl. *29*, 15–21. https://doi.org/10.1093/bioinformatics/bts635.

Figure 1: CRISPR screen identifies modulators of polyamine sensitivty

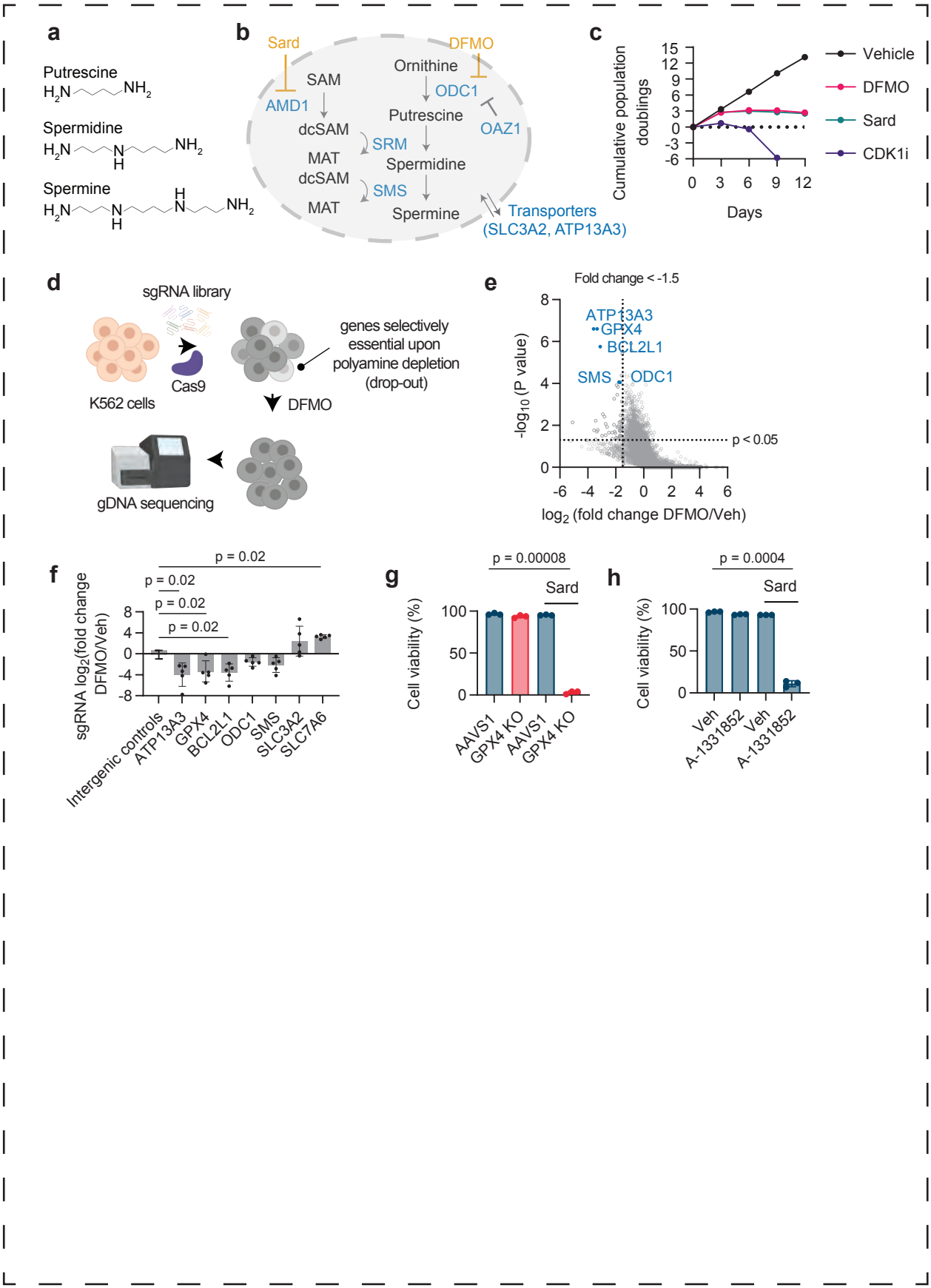

Figure 2: Polyamine depletion promotes ferroptosis

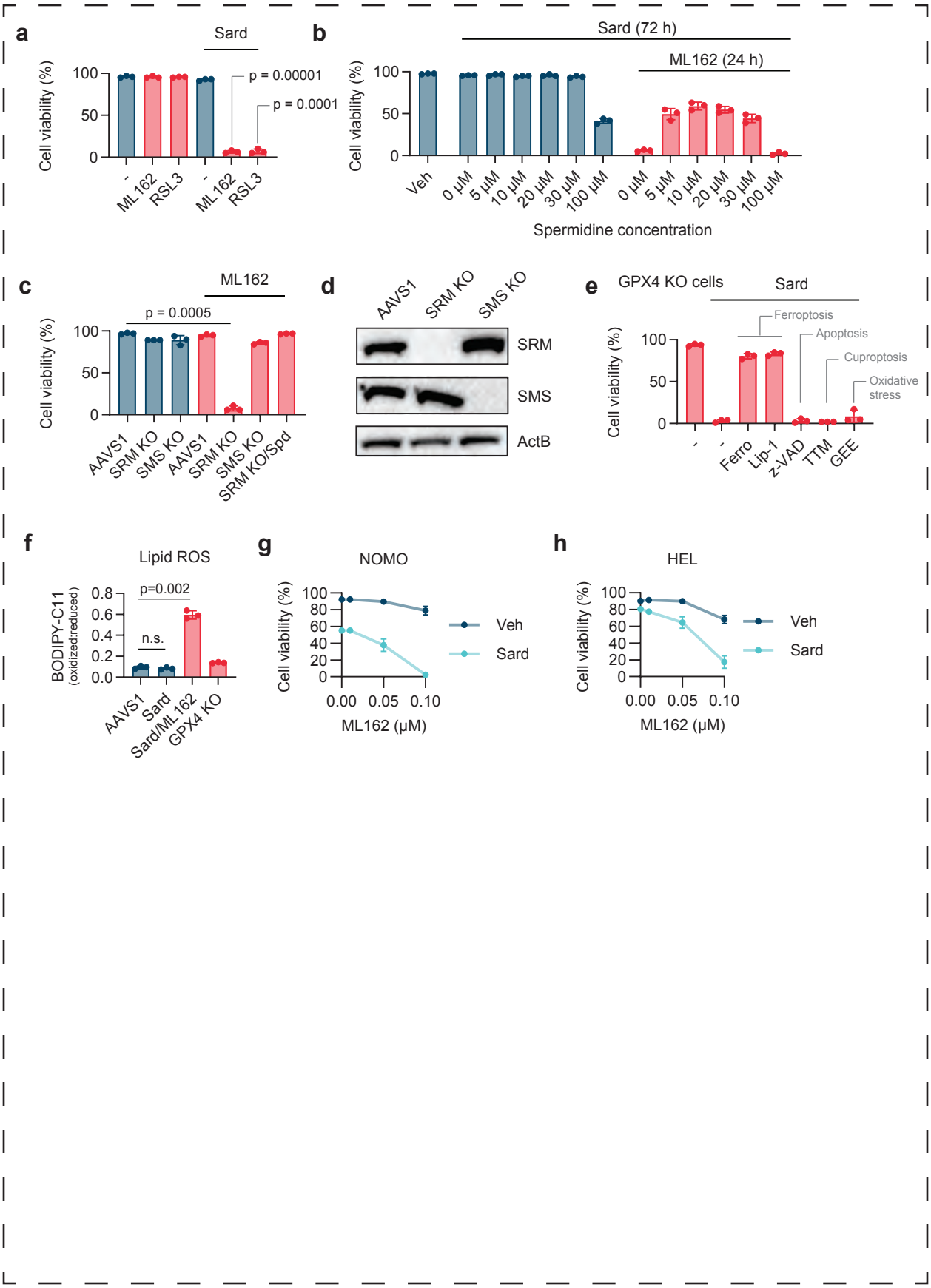

Figure 3: Polyamines act independently of major ferroptosis regulators

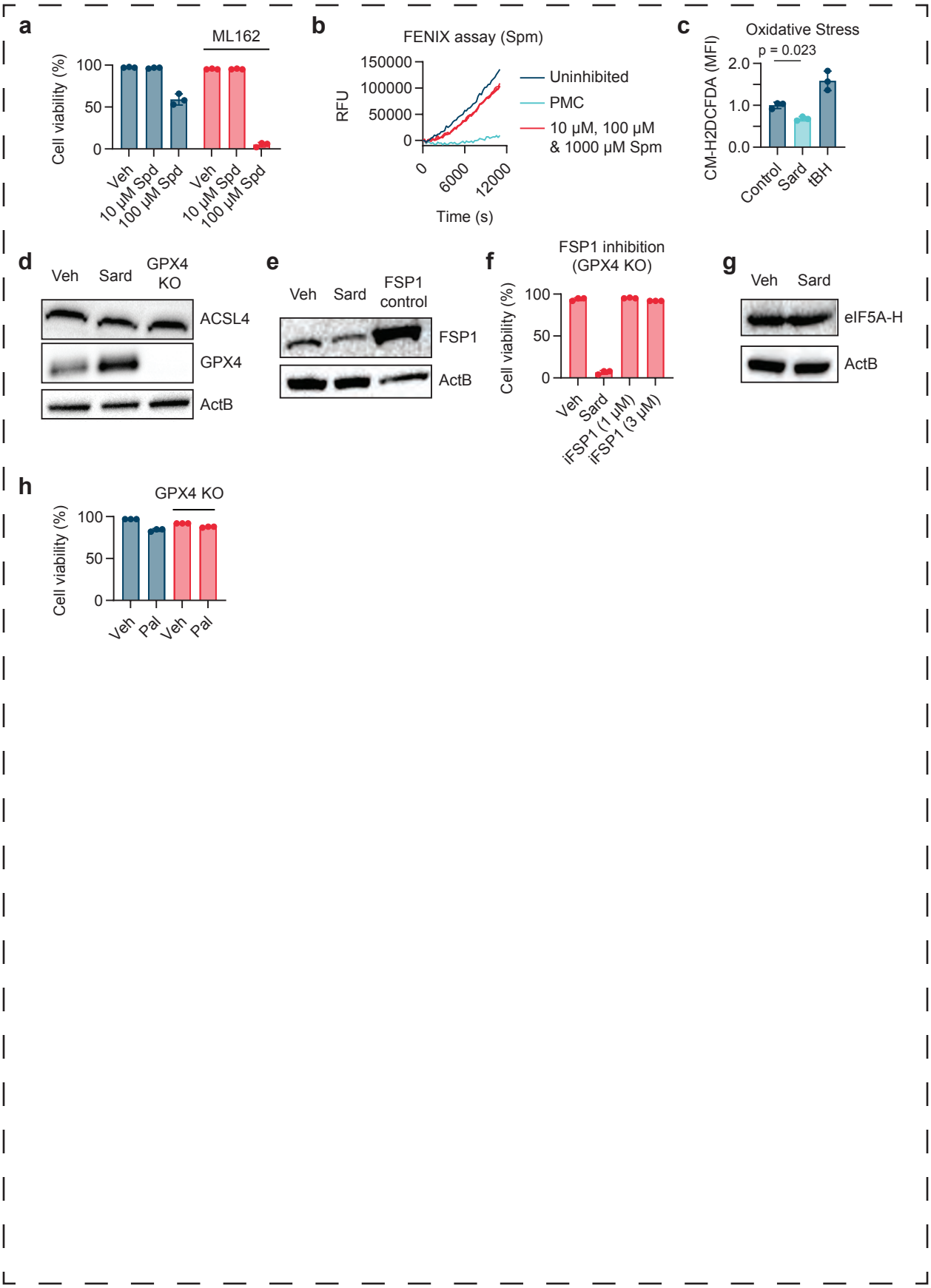

Figure 4: Polyamine deficiency increases redox-active iron

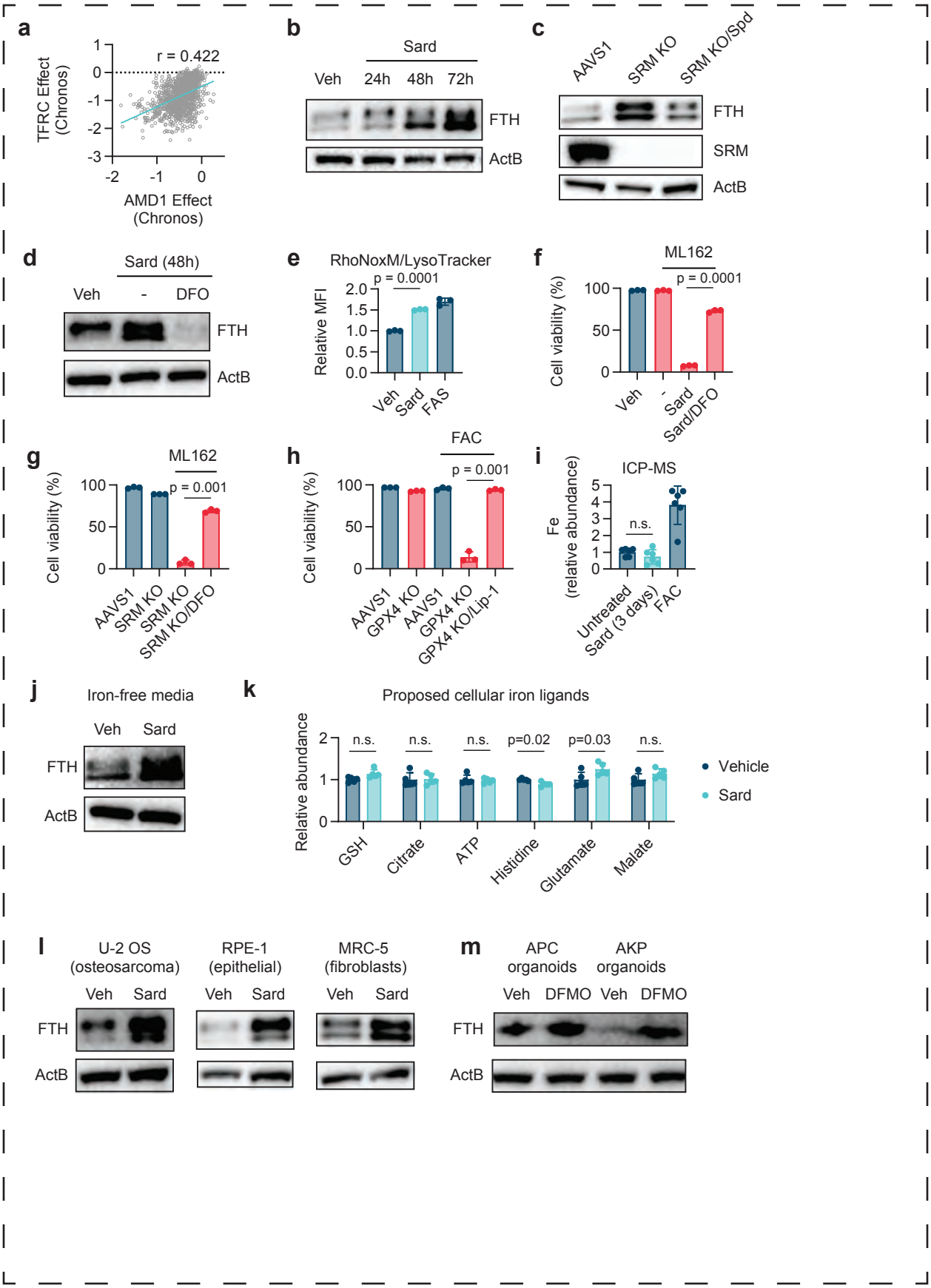

Figure 5: Genetically encoded sensor for redox-active iron

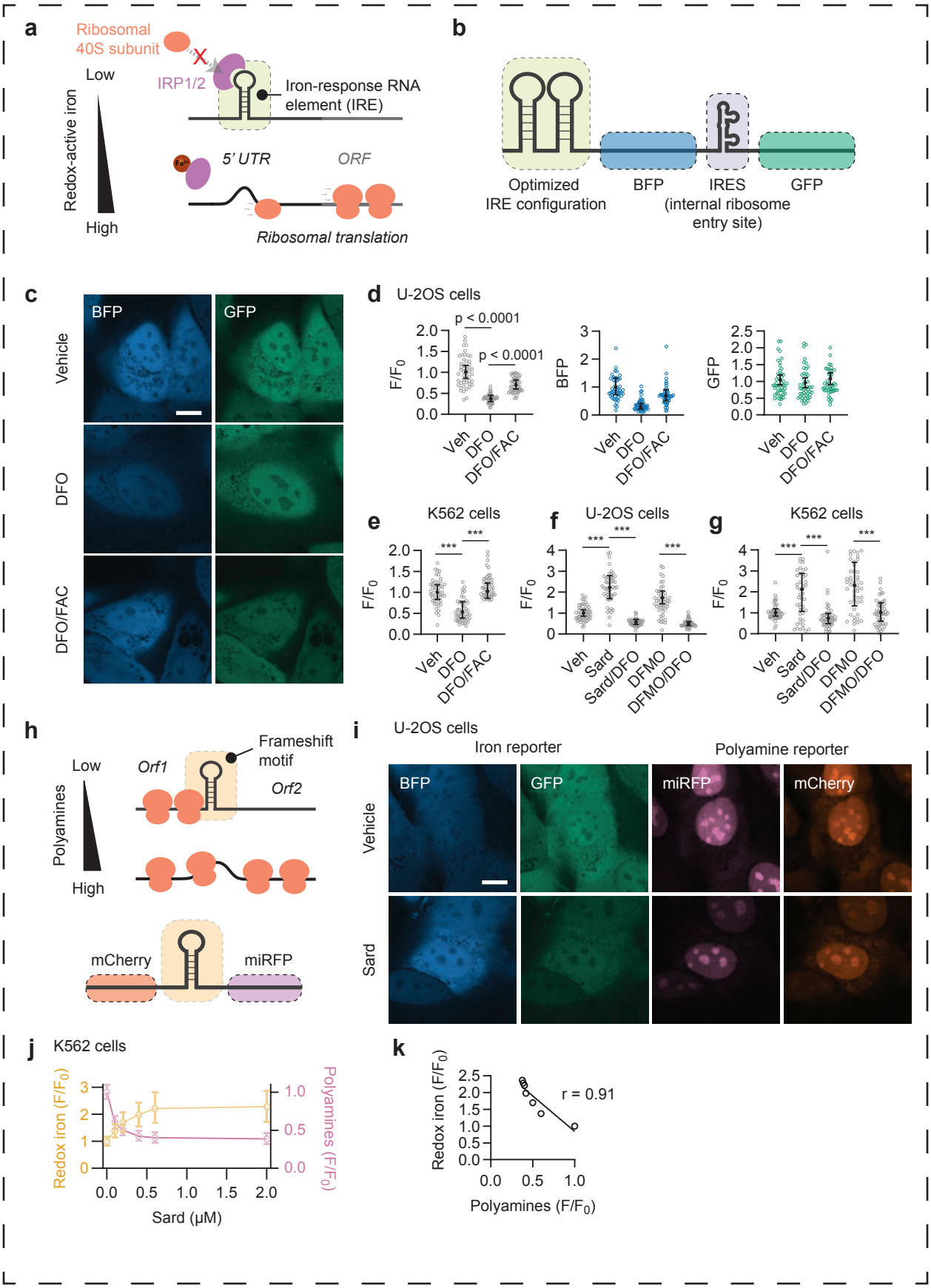
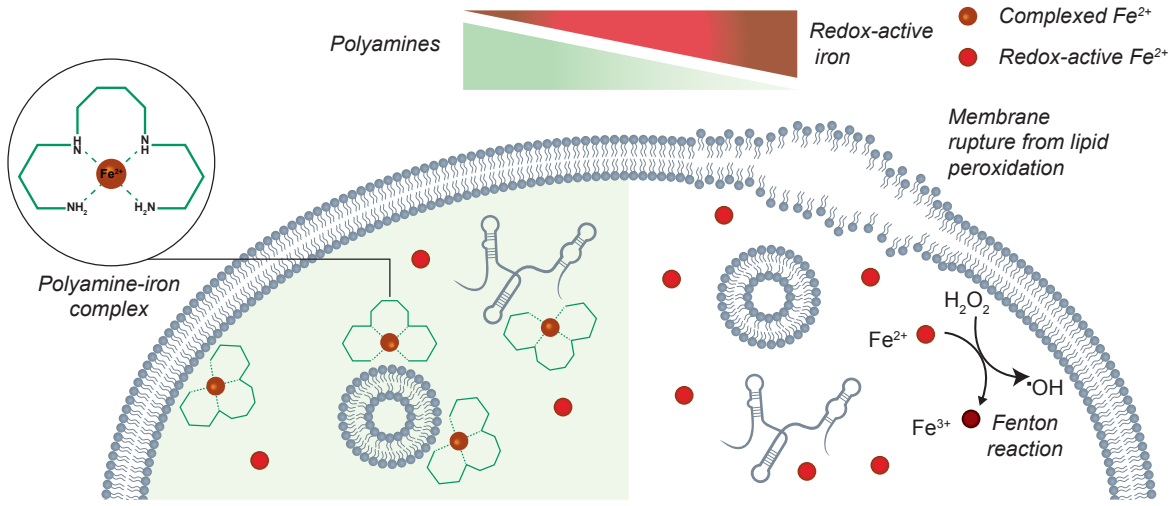
Figure 6: Polyamine depletion promotes ferroptosis